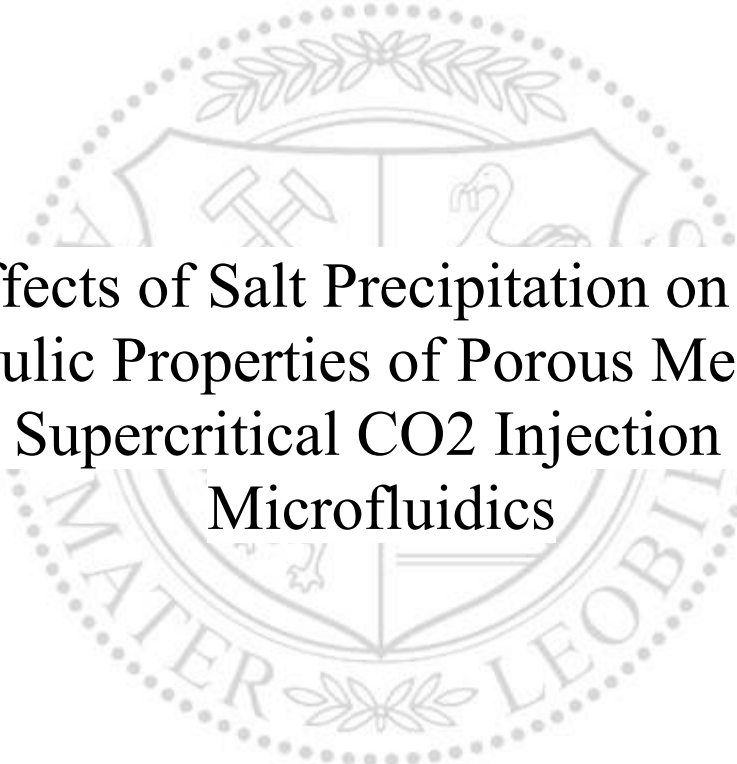




Department Petroleum Engineering

Master's Thesis



Effects of Salt Precipitation on the
Hydraulic Properties of Porous Media due
to Supercritical CO₂ Injection via
Microfluidics

Reagan Kabogozza

June 2022



MONTANUNIVERSITÄT LEOBEN
www.unileoben.ac.at

AFFIDAVIT

I declare on oath that I wrote this thesis independently, did not use other than the specified sources and aids, and did not otherwise use any unauthorized aids.

I declare that I have read, understood, and complied with the guidelines of the senate of the Montanuniversität Leoben for "Good Scientific Practice".

Furthermore, I declare that the electronic and printed version of the submitted thesis are identical, both, formally and with regard to content.

A handwritten signature in blue ink, appearing to read 'Reagan', written over a horizontal line.

Date 07.06.2022

Signature Author

Reagan Kabogozza

Kabogozza Reagan

Master Thesis 2022

Petroleum Engineering / Geoenergy
Engineering

Effects of Salt Precipitation on the Hydraulic Properties of Porous Media due to Supercritical CO₂ Injection via Microfluidics

Supervisor: Univ.-Prof. Dipl.-Phys. Dr.rer.nat.
Holger Ott

Co-supervisor/Advisor: Dipl.-Ing. Boris
Jammerneegg

Chair of Reservoir Engineering



I dedicate my thesis to my stepfather, Dr. mont . Rüdiger B. Richter.

Acknowledgements

I would like to acknowledge my advisor Dipl.-Ing. Boris Jammerneegg for the amount of time and work during the setup, design and running of the experiments. My gratitude also goes to laboratory technician Ing. Michael Koopmans who assisted me with the set-up and during the technical challenges of the experiments.

Abstract

Carbon Capture and Storage in deep saline aquifers (CCS) is one of the most favoured technical solutions for mitigating global CO₂ emission levels to achieve global CO₂ reduction goals and curb climate change. However, saline aquifers have highly mineralized brines whose minerals (salts such as halite, sylvite and others) precipitate during CO₂ injection due to the vaporization of the brine into the dry supercritical CO₂ phase. Salt precipitation can reduce the hydraulic properties of porous media, such as porosity and permeability, and cause major injectivity impairment or reduction, especially in the near-wellbore area where complete clogging has been reported to occur. This causes CO₂ storage operations to be less cost-effective, especially when a single well cannot accommodate the injection of several million metric tons of CO₂ per year. To correctly predict and simulate with the right clogging model how and when salt precipitation occurs during CCS in saline aquifers, understanding the physical mechanisms leading to and enhancement of salt precipitation is vital. It is also important to understand the nature of salt crystallization, the patterns of precipitation, and, therefore, the resulting change in hydraulic properties of porous media. Many ambiguities exist in the literature regarding the critical inputs into salt clogging models, and this has led to discrepancies in predictions of salt precipitation and what is observed in the field. This thesis examines salt precipitation on a microscopic level using lab-on-a-chip microchips to challenge some of these ambiguities and establishes what happens from a microscopic point of view. Air and dry supercritical CO₂ were injected into fully brine-flooded microchips to achieve complete drying under observation. Two types or forms of salt crystallization were observed to occur in different phases, while also having different patterns of salt precipitation. The influence of injection rate and brine salinity on the patterns and nature of salt precipitation is also examined. The obtained results were used to ascertain the amount of change in the hydraulic properties of the porous media (microchip) and then compared to the commonly used clogging models for salt precipitation simulation in saline environments.

Zusammenfassung

Die Kohlenstoffabscheidung und -speicherung in tiefen Salzwasseraquiferen (bekannt als CCS-Technologie) gilt als die am weitesten verbreitete technische Lösung zur Verringerung der globalen CO₂-Emissionswerte und um die globalen CO₂-Reduktionsziele zu erreichen und den Klimawandel zu begrenzen. Salzwasserleiter haben jedoch stark mineralisierte Solen, deren Mineralien (Salze wie Halit, Sylvit und andere) während der CO₂-Injektion aufgrund der Verdampfung der Sole in die trockene überkritische CO₂-Phase ausfallen. Salzausfällungen können die hydraulischen Eigenschaften poröser Medien wie Porosität und Permeabilität verringern und eine erhebliche Beeinträchtigung oder Verringerung der Injizierbarkeit verursachen, insbesondere in der Nähe des Bohrlochs, wo Berichten zufolge eine vollständige Verstopfung auftritt. Dies führt dazu, dass CO₂-Speichervorgänge weniger kosteneffektiv sind, insbesondere wenn ein einzelnes Bohrloch nicht die Injektion von mehreren Millionen Tonnen CO₂ pro Jahr aufnehmen kann. Um mit dem richtigen Verstopfungsmodell korrekt vorhersagen und simulieren zu können, wie und wann Salzausfällung während CCS in salzhaltigen Grundwasserleitern auftritt, ist das Verständnis der physikalischen Mechanismen, die zur Salzausfällung führen und diese verstärken, von entscheidender Bedeutung. Es ist auch wichtig, die Art der Salzkristallisation, die Niederschlagsmuster und die daraus resultierende Änderung der hydraulischen Eigenschaften poröser Medien zu verstehen. In der Literatur bestehen viele Unklarheiten bezüglich der kritischen Eingaben in Salzverstopfungsmodelle, und dies hat zu Diskrepanzen zwischen den Vorhersagen der Salzausfällung und den Beobachtungen im Feld geführt. Diese Master-Arbeit untersucht die Salzausfällung auf mikroskopischer Ebene unter Verwendung von Lab-on-a-Chip-Mikrochips, um einige dieser Widersprüche zu hinterfragen, und stellt fest, was aus mikroskopischer Sicht passiert. Luft und trockenes überkritisches CO₂ wurden in vollständig mit Sole überflutete Mikrochips injiziert, um eine vollständige Trocknung unter entsprechender Kontrolle zu erreichen. Es wurde dabei beobachtet, dass zwei Arten oder Formen der Salzkristallisation in unterschiedlichen Phasen auftreten, die auch unterschiedliche Muster der Salzausfällung aufweisen. Der Einfluss der Injektionsrate und des Salzgehaltes der Sole auf die Versuchs-Muster und die Art der Salzausfällung wird ebenfalls untersucht. Die erhaltenen Ergebnisse wurden verwendet, um das Ausmaß der Änderung der hydraulischen Eigenschaften des porösen Mediums (Mikrochip) zu ermitteln und dann mit den üblicherweise verwendeten Verstopfungsmodellen für die Salzausfällungssimulation in salzhaltigen Umgebungen zu vergleichen.

Table of Contents

Acknowledgements.....	v
Abstract.....	7
Zusammenfassung	8
Chapter 1.....	19
Introduction.....	19
1.1 Background and Context.....	19
1.2 Scope and Objectives.....	19
1.3 Achievements.....	20
1.4 Technical Issues.....	20
1.5 Overview of Master’s Thesis	21
Chapter 2.....	23
Literature Review.....	23
Introduction / Background	23
2.1	23
2.2 Mechanisms and physics of salt precipitation in saline aquifers during CO ₂ injection 27	
2.3 Macroscopic salt distribution.....	33
2.4 Sensitivity analysis on the magnitude and distribution of precipitated salt	35
2.5 Clogging modal and the Porosity-permeability relation	38
2.6 The divergence in literature and the missing link	40
2.7 Mitigation.....	41
Chapter 3.....	42
Experimental Apparatus.....	42
3.1 Apparatus	42
Chapter 4.....	48
Experimental setup, Procedure and Analysis	48
4.1 Preliminary Experiment	48
4.2 Primary Experiments	49
Chapter 5.....	55
Results and Discussion	55
5.1 Preliminary Experiments Results and Discussion.....	55
5.2 Main Experiment Results and Discussion	66
Chapter 6.....	71
Conclusion	71
6.1 Summary	71
6.2 Evaluation	72
6.3 Future Work.....	72

Chapter 7.....	74
References.....	74
References.....	78

List of Figures

Figure 1: Showing the Carbon Stocks in various reservoirs and the corresponding fluxes between the reservoirs 10^{15} g C and 10^{15} g C y^{-1} . The surface and Geological Carbon cycle in green shows the residence time of CO ₂ in the atmosphere and in the underground. Carbon Capture and Storage underground has the capacity to effectively store CO ₂ in the atmosphere for 10^9 years. Adopted from (Carlson et al., 2009; Hannah, 2015; Steele et al., 2009)	24
Figure 2: Showing the trapping mechanisms of CO ₂ and their trapping time scales, (Christian Hermanrud, 2009)	25
Figure 3: a) Showing viscous two-phase displacement of Brine by CO ₂ , a viscous pressure gradient due to injection of CO ₂ , a capillary pressure develops in the porous media due to saturation differences in areas where residual brine exists and where displacement has not happened yet. b) Saturation differences increase, capillary pressure gradient also increases, the evaporation is happening while the drying front (precipitation) starts. The formed salt is porous, and its capillary pressure enhances the capillary pressure gradient, which overcomes the viscous pressure gradient. This causes brine backflow. c) The strength of currents is observed in experiments by currents and counter currents. d) Capillarity of salt drives more brine on salt films causing self-enhancement of the salt as more drying happens. e) Salt self-enhancement causes salt to grow further into CO ₂ pathways, which leads to complete pore throat plugging in some areas.	30
Figure 4: Real-life experiment salt images a) Showing the two salt crystal formation configurations in microfluidics chips. Large salt crystals and the aggregates salt crystals (Ho and Tsai, 2020). b) Showing the hydrated salt aggregate crystals indicating the hydrophilic nature of the salt (Miri et al., 2015).	32
Figure 5: Visualization of a local salt precipitation due to a stabilized drying front. Brine is continuously brought to the salt drying zone causing more precipitation	34
Figure 6: Visualization of the homogeneous salt precipitation. Salt precipitation is mostly where residual brine is located. CO ₂ flow paths are left salt free	35
Figure 7: Showing a comparison between a derived modal for salt precipitation taking into account polycrystalline salt aggregates and other commonly known models. None of the models can closely predict the hydraulic characteristics change (Masoudi et al., 2021).....	39
Figure 8: Visualization of the microfluidics model of a physical porous rock from a limestone sample, (MICRONIT, 2021).....	42
Figure 9: Showing a chip holder on the left and a high-pressure connection setup with fittings and ferrules on the right used in the experiments, (MICRONIT, 2021)	44
Figure 10: The Motic AE2000 inverted microscope with a mounted digital camera and Monitor, (MOTIC).....	44
Figure 11: Image of the Chemyx fusion 6000 high-pressure pump, (CHEMYX, F. 6.-X., 2022).....	45
Figure 12: Chemyx stainless steel syringes specification, (CHEMYX, 2022).....	45
Figure 13: The keller pressure transducer, Series PRD-33X, (KELLER AG für Druckmesstechnik, 2021)	46
Figure 14: Equibar back pressure regulator used in the experiments, (Fluid Controls Ltd, Dec 22)	47
Figure 15: The Leister Hot air blower with the Mistral 6 system, (Leister Technologies AG, 2021).....	47
Figure 16: Showing the schematic setup of the experiments carried out.....	50
Figure 17: Showing the desired path from liquid CO ₂ in the bottle to Supercritical CO ₂ in the microchip	52
Figure 18: Showing the mage of the Area Of Interest for the main experiment.....	53
Figure 19: Images of Microchip with polycrystalline salt precipitation as irregular random patterns, A and B. Also shown is the crystallization before self-enhancement, C.....	57
Figure 20: Showing Dendritic shape patterns of the polycrystalline salt.....	58

Figure 21: Showing the growth of random shaped salt polycrystalline aggregates in the dry air phase 59

Figure 22: Images showing the growth and development of dendritic shaped salt aggregates and large cubic salt crystals 60

Figure 23: Showing the microscope focus at the top and bottom of the microfluidics edging depth. The precipitation that shows a change in sharpness from top to bottom is indicated by the red arrows and the precipitation that does not cover the entire microfluidics chip edging depth. The aggregates, for example in the red circle, are salt crystals crammed together and occupying different vertical positions. Sharpness changes for various crystals. The very dark aggregates occupy the entire edging depth 61

Figure 24: Showing at the top the mask of the salt-free image, and the salt precipitated image at the bottom 62

Figure 25: Showing the representation of the salt at different Threshold cut off values. The light greys representing the salt that does not cover the entire edging depth is eliminated in Image C..... 63

Figure 26: Showing the added images A, the resulting 8-bit image B, and finally the binary image C after applying appropriate cut off values in the Threshold. The porosity decreased from 60% to 39%, a 65% decrease in porosity due to salt precipitation..... 64

Figure 27: Showing the multi-rate pressure responses and slope used to calculate the permeability of the clean and salt-precipitated microchip 65

Figure 28: AOI at beginning of CO₂ injection cycles after Brine flooding 67

Figure 29:AOI at the End of the experiment. Complete dry out, 23,456PV injected 68

List of Tables

Table 1: The dimensions of the physical network microchip (MICRONIT, 2021).....	43
Table 2: Showing the summary of data used to calculate the permeability of the microchip when distilled water is the working fluid.....	55
Table 3: Showing the porosity of a fresh, clean microchip and that of a microchip after salt precipitation	64
Table 4: Showing the summary of data used to calculate the permeability of the microchip when liquid CO ₂ is the working fluid	66

Nomenclature

k	permeability	$[m^2]$
$^{\circ}C$	Degrees Celsius	
L	Length	m
D	Darcy	
mD	millidarcy	

Abbreviations

AOI	Area Of Interest
CCS	Carbon Capture and Storage
CO ₂	Carbon di Oxide
ml/hr	Millilitre per hour
Nacl	Sodium Chloride
ppm	Parts per million
°C	Celsius degrees

Chapter 1

Introduction

1.1 Background and Context

Saline aquifers host highly mineralised brines whose minerals particularly salts precipitate during CO₂ injection due to the vaporisation of the brine into the dry supercritical CO₂ phase. Salt precipitation may reduce the hydraulic properties of porous media, such as porosity and permeability. A decrease in the hydraulic properties causes significant injectivity impairment or reduction, especially in the near-wellbore area where complete clogging has been reported to occur. This causes CO₂ storage operations to be less cost-effective, especially when a single well cannot accommodate the injection of several million metric tons of CO₂ per year. Previous works have been done on salt precipitation in porous media, but much has been done on rock cores and less at the microscopic level. Also, a lot of ambiguity exists in the literature on the effective porosity change and permeability of porous media. This thesis will seek to establish the spatial location of precipitated salt in the micromodel, the pattern of precipitation, the hydraulic properties effects and if the salinity of the brine has a relationship to these factors.

1.2 Scope and Objectives

In this thesis, two experiments were run to investigate salt precipitation in a saline environment. One preliminary experiment used air to dry the brine without the high temperature and pressure reservoir conditions, and the primary experiment used supercritical CO₂ under reservoir conditions. The thesis intends to prove the relationship between brine salinity and the amount of salt precipitation, the pattern of crystallisation, and the change in micromodel hydraulic properties, such as porosity and permeability. On a microscopic level, the manner of salt precipitation will be examined. The understanding of if and when salt

forms polycrystalline aggregates, singular or aggregates of cubic salt crystals or simply thin coatings on porous media grains will help to prove the existence of an effective porosity reduction and hence, permeability. Experimental conditions which allow identifying whether the precipitated salt is intrinsically permeable will be examined.

1.3 Achievements

An experiment setup design for this experiment was built and demonstrated that it would achieve the desired investigational work with a few technical twitches.

The preliminary experiments demonstrated that salt precipitation is achieved when dry air (gas) is continuously introduced into a saline porous medium. Mechanisms like Two-phase displacement of brine away from the injection point, evaporation of residual brine into the displacing phase, molecular diffusion of dissolved salt into the aqueous phase, and salt self-enhancing lead to and contribute to salt precipitation in the drying/displacing phase. Different natures of salt precipitation (polycrystalline or cubic salt crystals) were observed, and the dependence of nature on the phase in which the salt precipitated was examined. Patterns of salt precipitation were observed, and their dependency on the rate of CO₂ injection and salinity was established.

1.4 Technical Issues

High-pressure and high-temperature microfluidic experiments are challenging and especially microfluidic flooding with supercritical CO₂. This may be the reason that there are just very few CO₂ microfluidic experiments reported in the literature. CO₂ is very volatile and leaks from the high pressure and temperature equipment to the environment which is very difficult to avoid, find and fix. Leakage may lead to pressure imbalances, which can be an issue for sensitive equipment, like pressure transducers, which get easily damaged in the process. This was experienced during the present MSc project, and it leads to a time and budget loss.

Vaporizing water in a supercritical CO₂ phase requires the injection of several thousand pore volumes, which is different to a classical displacement experiment, where only a small number of pore volumes are injected. Classical high-pressure microfluidic pumps have naturally a small volume, which required frequent refills. This is not a problem for the experiments, since the water phase is immobile, but increases the chances for pressure imbalances and hence failure. This problem could be solved with classical dual-piston pumps, but those are typically not pulse-free as pumps specifically designed for microfluidics and are not as precise.

In summary, setting up, testing and commissioning such a setup is demanding and it is an achievement in itself as other novel steps in scientific research.

1.5 Overview of Master's Thesis

In this master's thesis, the background on the importance and state of the art technology of CSS (Carbon Capture and Storage), including the challenges in saline environments, are discussed in the literature in Chapter 2. The mechanisms of salt precipitation, previous simulation work on porous cores and aquifer-on-a-chip experiments for CCS experiments are revisited. The current ambiguities in the literature are identified and, therefore, the shortcomings of the clogging models used for numerical simulations.

The experiment apparatus and software used are fully described and illustrated with images in 0. The setup design and procedure of preliminary and primary experiments are fully described in Chapter 4. Chapter 5 discusses the obtained results of the preliminary and primary experiment. The nature of salt precipitation, the salt patterns formed, the phase in which the salt precipitates and the influence of rate and salinity on salt precipitation are discussed. Hydraulic property changes of the porous media were also investigated. The technical problems of the primary experiment are also explained.

Chapter 2

Literature Review

2.1 Introduction / Background

Carbon dioxide (CO₂) is one of the leading greenhouse gases contributing to global warming, and therefore, understanding the Carbon Cycle is very important. The global carbon cycle refers to the exchange and flux of carbon between and within four sinks (reservoirs) which are also major components of the Earth system; namely the atmosphere, lithosphere, biosphere, and hydrosphere (Carlson et al., 2009; Hannah, 2015; Steele et al., 2009).

Without human activities, the sum and exchange of carbon within these sinks is maintained in a near steady-state condition by slow natural processes. Anthropogenic sources like burning fossil fuels, deforestation, cement manufacturing, etc., have significantly altered the exchange rates leading to alarmingly more carbon flux, especially in the atmosphere (Carlson et al., 2009; Hannah, 2015; Steele et al., 2009).

CO₂ and Methane (CH₄) contribute to the natural greenhouse effect that has helped maintain enough warmth on Earth to support life. However, in the last 200 years since the emergence of the industrial age, human activities have increased the atmospheric mass of CO₂ from 280 ppm to 360 ppm today, with an increase of 25% in the last century alone (Bates, 2019). This has enhanced the greenhouse effect and is quickly warming up the Earth. Current energy scenarios show that if processes that add CO₂ to the atmosphere are not curbed, temperatures will continue to rise in kind (Arnell et al., 2011). Because human activities helped to put most of the CO₂ into the atmosphere in the last 200 years, it is imperative that we proactively try to reduce the further release of CO₂ into the atmosphere (Carlson et al., 2009; Hannah, 2015; Steele et al., 2009).

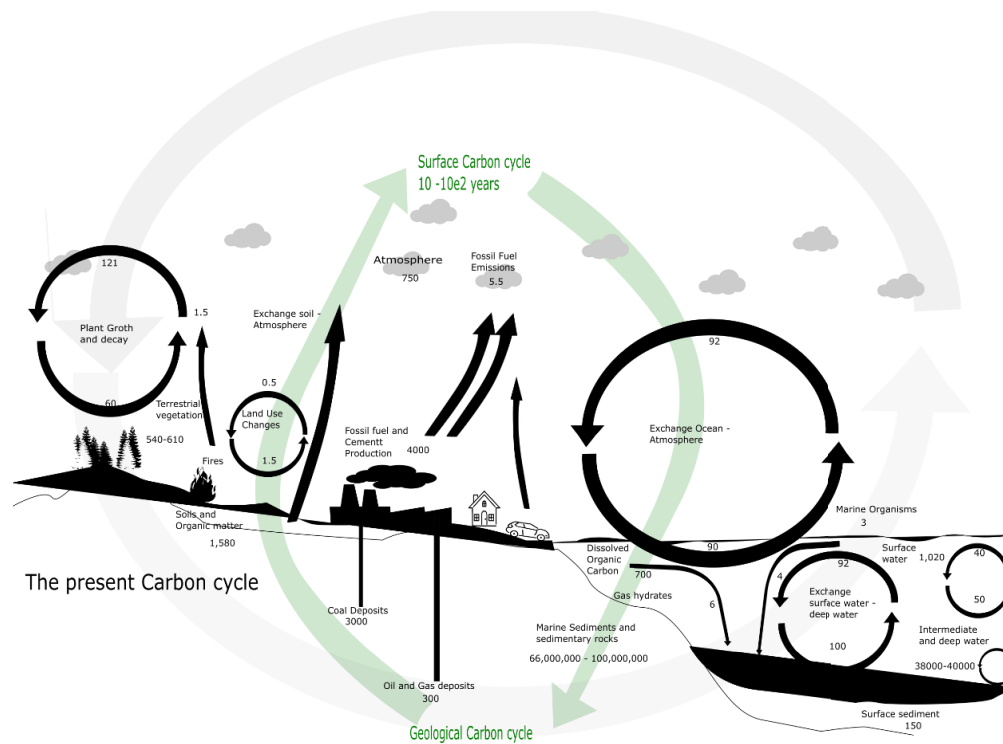


Figure 1: Showing the Carbon Stocks in various reservoirs and the corresponding fluxes between the reservoirs 10^{15} g C and 10^{15} g C y^{-1} . The surface and Geological Carbon cycle in green shows the residence time of CO_2 in the atmosphere and in the underground. Carbon Capture and Storage underground has the capacity to effectively store CO_2 in the atmosphere for 10^9 years. Adopted from (Carlson et al., 2009; Hannah, 2015; Steele et al., 2009)

Carbon capture and storage (CCS) is the capturing carbon from anthropogenic sources such as power generation, transportation, industrial sources, chemical production, petroleum production, etc. and storing it in underground carbon reservoirs. This carbon is expected to remain in such underground reservoirs for up to a trillion years before natural geologic processes trap it permanently (Intergovernmental Panel on Climate Change, 2005).

CO_2 is trapped in reservoirs through structural and stratigraphic trapping, capillary trapping of residual CO_2 , Solubility trapping where CO_2 dissolves in reservoir brine, and mineral trapping where CO_2 reacts with some minerals and form other minerals. All these mechanisms have varying trapping time scale with structural and strategic trapping happening at injection to mineral trapping happening after ten of thousands of years, see Figure 2 below.

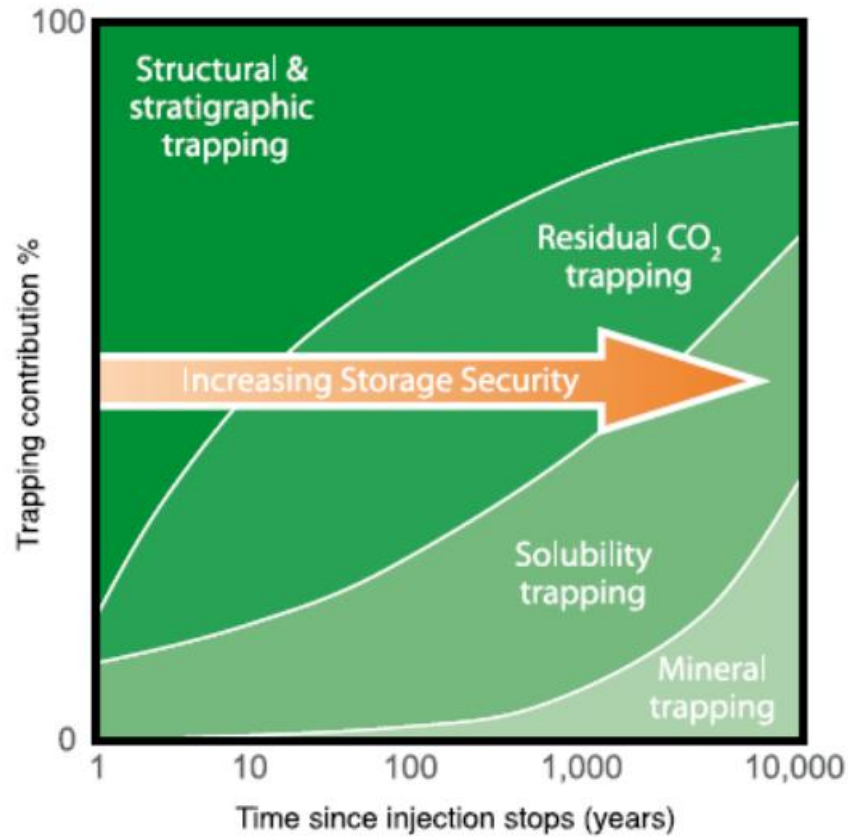


Figure 2: Showing the trapping mechanisms of CO_2 and their trapping time scales, (Christian Hermanrud, 2009)

The Intergovernmental Panel on Climate Change (IPCC) defines Carbon dioxide (CO_2) capture and storage (CCS) as the extraction of CO_2 from industrial and energy-related processes, transportation, and long-term isolation. Among the potential carbon reduction and long-term isolation methods include: (Intergovernmental Panel on Climate Change, 2001, 2005);

1. Reduce energy demand by improving energy utilization efficiency.
2. Decarbonising energy supplies by either switching to less carbon-intensive fuels (for example, coal to natural gas) or expanding the use of renewable and nuclear energy sources.
3. Storage in Geological formations and use in Enhanced Oil Recovery (EOR). Indeed, geologic carbon storage is an imitation of how nature has stored CO_2 for millions of years before. The Pisgah field, which naturally contains tremendous amounts of CO_2 , in Mississippi, for example, was discovered by Shell in 1960 (Keith Bowman, 2016).

4. Deep ocean or sea floor storage as liquid CO₂, injection in gas hydrates or below the sea floor in tight basaltic rocks ("reservoirs"). However, there are concerns about ocean acidification and interaction with marine life.
5. Industrial fixation of CO₂ into inorganic carbonates

The above portfolio of known technological options can achieve a significant atmospheric CO₂ stabilisation. However, no single solution will be able to provide all of the required emissions reductions, and therefore a combination of solutions should be explored. (Intergovernmental Panel on Climate Change, 2005). As a result, CCS is critical in the mix of solutions for reducing CO₂ levels in the atmosphere.

There are several potential geological formations for storing carbon dioxide, including depleted oil and gas reservoirs, coal seams, and deep saline aquifers. Deep saline aquifers are known to have the biggest potential in terms of storage capacity (Intergovernmental Panel on Climate Change, 2005).

CCS in deep saline aquifers is a highly favoured solution for the mitigation of global CO₂ emission levels to achieve global CO₂ reduction goals and curb climate change. Several pilot plants and commercial-scale field demonstrations have shown positive results, with the latter achieving injection of up to 1 million metric tons of CO₂ per year (Kim et al., 2012, p. 398).

Examples of successful projects for CCS include but are not limited to, Ketzin in Germany (Kießling et al., 2010), Weyburn in Canada (Preston et al., 2005), Sleipner and Snohvit in Norway (Maldal and Tappel, 2004; Torp and Gale, 2004), Nagaoka in Japan (Mito and Xue, 2011), In Salah in Algeria (Green house gas control technologies, 2003; RIDDIFORD et al., 2003) and Frio in Texas (Hovorka et al., 2006), and Quest in Canada (Shell).

However, the candidate formations have taught an important lesson that cannot be ignored. They have highly mineralised brines whose minerals (salts like Halite) precipitate during CO₂ injection due to vaporisation of the brine into the CO₂ phase (Bette and Heinemann, 1989; Miri and Hellevang, 2016). Precipitation reduces porosity and permeability, and this causes major injectivity impairment problems. Injectivity reduction is considered so vital that it could make such projects cost-ineffective, as more wells would need to be drilled if the injection of several million metric tons of CO₂ per year within a single well cannot be achieved (Kim et al., 2012, p. 398) (Miri et al., 2015) (Peysson, 2012). Some investigators have noted that porosity reduction, however modest it may sometimes be, can generate dramatic reductions in permeability of up to 75% (Bacci et al., 2011; Ott et al., 2011; Ott et al., 2015) and sometimes complete clogging. The effects are more pronounced near the injection well, reducing injectivity (Bacci et al., 2011; Miri et al., 2015).

Field projects of gas storage (injection) and production from geological formations, especially with saline brines, have confirmed pressure buildup attributed to salt formation sometimes occurring very early in the project's life span (Bette and Heinemann, 1989; Jasinski et al., 10051997; Kiessling et al., 2010; Kleinitz et al., 2003; Maldal and Tappel, 2004; Torp and Gale, 2004).

Laboratory experiments using

1. Core-flooding (injecting cores with brine and CO₂, Nitrogen or air) experiment methods have shown salt precipitation and the consequential porosity and permeability impairment probable during CO₂ injection in the CCS process (Pruess and Müller, 2009) (Ott et al., 2011; Ott et al., 2021) (André et al., 2014; Bacci et al., 2011; Oh et al., 2013). Or
2. Microchips (Aquifer-on-a-chip experiments) flooded with brine, and later gas injection have been used to show and explain salt formation. They are available in various fabrications in well-defined homogeneous or random micropatterns or structures. They provide direct pore-scale visualisation and insights into salt precipitation mechanisms at the microscale. (Kim et al., 2013; Miri et al., 2015)

Other evidence for salt precipitation is the analytical and numerical simulation of idealised 1D and 2D-radial systems (André et al., 2014; Giorgis et al., 2007; Kim et al., 2012; Meng and Jiang, 2014; Muller et al., 2009; Wang and Liu, 2013; Y. Wanga et al., 2010).

2.2 Mechanisms and physics of salt precipitation in saline aquifers during CO₂ injection

Injection of CO₂ in saline aquifers displaces brine in the form of two-phase displacement until residual (irreducible) brine remains as thin films on porous media grains. Then there is a water mass transfer mainly from the aqueous brine phase to the gaseous CO₂ phase. This is because the water vapour in the CO₂ has low partial pressure and has to equilibrate with the aqueous phase. Even if the solubility of water in supercritical CO₂ is very low, continuous injection of CO₂ will lead to gradual brine vaporization. Brine vaporization then leads to an increase in ion concentration in the brine and eventually complete formation dry-out, especially a few meters close to the injection well (André et al., 2014; Bacci et al., 2013; Giorgis et al., 2007; Ott et al., 2011; Peysson, 2012, 2012; Pruess and Müller, 2009).

2.2.1 Macroscopic and microscopic mechanisms

Researchers have identified several physical factors by which salt precipitates and is enhanced. Through core flooding experiments, micro-fluidics and numerical simulations, these physical mechanisms were identified to occur at a different time and length scale (Miri and Hellevang, 2016; Pruess and Müller, 2009). They include:

1. Two-phase displacement of brine away from the injection point by CO₂ leaving behind residual brine,
2. Vaporation of the residual brine into the CO₂ phase,
3. Gravity bypass of CO₂ (gravity effects due to buoyancy),
4. Backflow of brine towards the injection point due to capillary pressure gradient exceeding viscous pressure gradient
5. Molecular diffusion of salt into the brine aqueous phase,
6. Salt self-enhancing

Miri et al. (2016) give a detailed description of these mechanisms (Miri and Hellevang, 2016). They suggest that just after the start of CO₂ injection, a two-phase-flow zone forms where both an aqueous phase of brine and a CO₂-rich phase are present. There is a two-phase displacement leading to primary drainage of brine away from the injection well or point. This is due to the viscous displacement of brine by CO₂. A zone is left behind where liquid brine is trapped in a variety of configurations, such as wetting films surrounding grain surfaces, liquid bridges and pools of brine between pores. The region with residual water is exposed to low vapour pressure flow of dry CO₂, which launches an evaporation process. The solubility of water in supercritical CO₂ is several orders of magnitude smaller than the solubility of CO₂ in brine. However, a significant amount of water will evaporate into the CO₂ stream under persistent CO₂ flow, resulting in a formation dry-out. The dry-out front forms and moves at a much slower velocity than the CO₂ flooding front. Indeed, water is removed from the vicinity of the injection site or point by both two-phase displacement and evaporation. However, time scales are well separated. Essentially, there is only a little evaporation during two-phase displacement, and there is also no convective flow during dry-out (André et al., 2014; Ott et al., 2011; Ott et al., 2014; Ott et al., 2021).

Because most of the water exchange occurs in the dry-out zone, a saturation gradient across the drying front is created (André et al., 2014). This saturation gradient is much greater than the saturation gradient created in the case of a pure viscous displacement. This in turn creates a capillary gradient. The resulting capillary pressure gradient eventually overcomes the injection pressure gradient and drives the brine toward the evaporation front (in the direction of the injection well or point). This brings more salt ions (in brine) towards the evaporation

front, which precipitate as the fresh brine evaporates (André et al., 2014; Ott et al., 2011; Ott et al., 2015; Pruess and Müller, 2009).

As the water is evaporated (dissolved) into the CO₂ stream, the salt concentration in the trapped brine increases, resulting in salt diffusion into the remaining brine (Pruess and Müller, 2009; Shahidzadeh-Bonn et al., 2008). Once the salt concentration reaches its solubility limit and brine becomes supersaturated owing to the evaporation, salt will precipitate out of the solution. The precipitated salt is hydrophilic in nature and can effectively imbibe fresh brine from long distances to the evaporation front, resulting in further precipitation. Miri et al. (2016) note that the nature of this mechanism is more or less the same as that of the capillary pressure gradient described above, but with different origins (Miri and Hellevang, 2016). In addition, capillary flow due to salt is much stronger and gives significant stability to the water films, thereby enhancing salt precipitation (Pruess and Müller, 2009). However, some but not all of these mechanisms have been observed in microfluidic chip experiments.

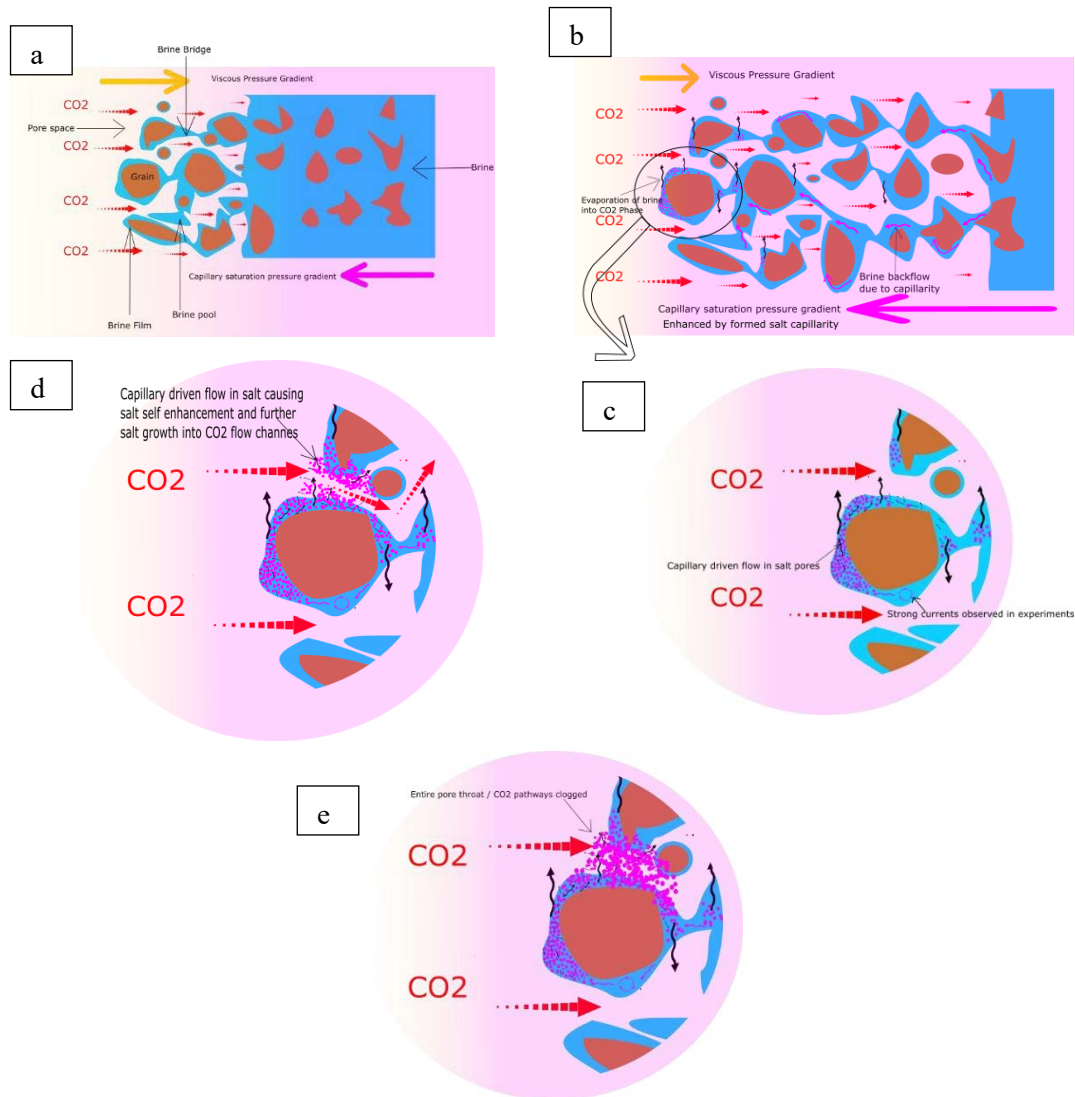


Figure 3: a) Showing viscous two-phase displacement of Brine by CO_2 , a viscous pressure gradient due to injection of CO_2 , a capillary pressure develops in the porous media due to saturation differences in areas where residual brine exists and where displacement has not happened yet. b) Saturation differences increase, capillary pressure gradient also increases, the evaporation is happening while the drying front (precipitation) starts. The formed salt is porous, and its capillary pressure enhances the capillary pressure gradient, which overcomes the viscous pressure gradient. This causes brine backflow. c) The strength of currents is observed in experiments by currents and counter currents. d) Capillarity of salt drives more brine on salt films causing self-enhancement of the salt as more drying happens. e) Salt self-enhancement causes salt to grow further into CO_2 pathways, which leads to complete pore throat plugging in some areas.

2.2.1.1 A view on mechanisms observed in microfluidics

Miri et al. (2015) only observed three flow regimes or mechanisms leading to and during salt precipitation in microfluidics chips (Miri et al., 2015). They observed the usual two-phase displacement of brine by the injected dry CO₂ gas phase. This mechanism happens very fast. Then followed by the evaporation regime, which is a slow mechanism (up to 24 hours at low injection rates of 0.5 ml/min; approximately equivalent to field injection rates). Lastly, was the salt precipitation at the maximum salt concentration in the brine. A drying front was formed in the chip and propagated in the direction of flow. The propagation was relatively rapid, reaching the end of the microchip in just 12 minutes.

After the two-phase displacement, Miri et al. (2015) noticed the residual water saturation had various configurations, which they reckon is influenced by the capillary pressure of the porous media (Miri et al., 2015). Configurations seen include films around grains, domes, pools and liquid bridges, which evolved with time as evaporation occurred (Ho and Tsai, 2020; Miri et al., 2015).

After the salt precipitation, they estimated that salt covered 23% of the pore network volume. However, this is probably not covering the entire depth of the chips since minimal pressure drop was noticed across the chip, indicating little permeability change. The conclusion, therefore, is that in some places, precipitation occurred just as a surface coating mechanism. A more accurate determination of the thickness of the salt was not possible, and so the intensity of the salt colouring was used to estimate the vertical salt coverage.

The salt was observed to precipitate in two forms or configurations (Kim et al., 2013; Miri et al., 2015; Miri and Hellevang, 2016):

1. Relatively large crystals grow in the aqueous phase. This was observed to happen in liquid bridges (before liquid thinning begins) or pools and at low injection/evaporation rates where there was sufficient time for crystal growth and formation. These were also observed by Martin Ho et al. (2020), who noted that large bulk crystals, with a transparent and ordered cubic structure, nucleate first via the self-assembly process of salt ions in the liquid phase when the ion concentration exceeds the solubility under certain thermodynamic conditions (Ho and Tsai, 2020).
2. Disordered salt crystal aggregates of micro-meter size (polycrystalline aggregates) form in the gas phase. These are enabled by the hydrophilic nature of the salt, in that the formed salt has thin water films, which in turn attract more water from the adjacent pore grain brine films (Ho and Tsai, 2020). In addition to the inter-connected thin brine film on the formed salt and pore grains, it is believed that the salt has narrow pores, which significantly multiplies its capillarity. This enables continuous

imbibition of fresh brine over long distances to the evaporating front, thus allowing the continuous growth of salt on these aggregates into the CO₂ phase pathways. A mechanism they called self-enhancing nucleation and precipitation (Ho and Tsai, 2020).

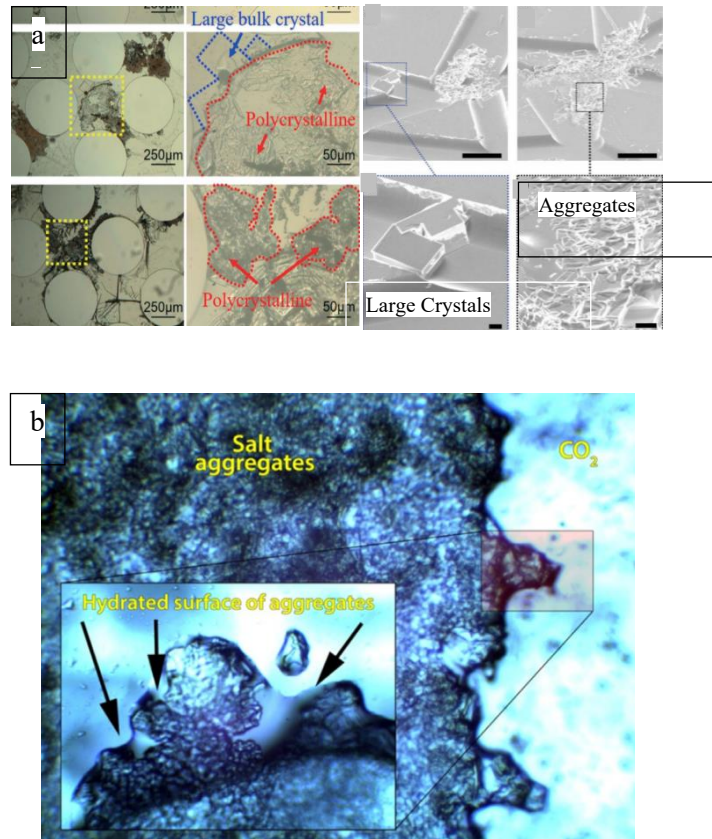


Figure 4: Real-life experiment salt images a) Showing the two salt crystal formation configurations in microfluidics chips. Large salt crystals and the aggregates salt crystals (Ho and Tsai, 2020). b) Showing the hydrated salt aggregate crystals indicating the hydrophilic nature of the salt (Miri et al., 2015).

Miri et al. (2015) suggest that the capillary pressure in the salt induces very fast high convective forces in the brine films enabling more salt formation than just the evaporation of the brine films on pore grains would precipitate (Miri et al., 2015). The effect can happen because the velocity of capillary transport to the evaporation zone is higher than the evaporation rate, even at very high flow rates. For this reason, they suggest that laboratory experiments and numerical simulations for salt precipitation should consider brine being transported from outside of the drainage area. Indeed, Ott et al. (2011) suggest that the finite sample size of experiments makes a finite brine volume, hence underestimating the magnitude of salt precipitation (Ott et al., 2011). With this brine backflow (capillary backflow) model, it is possible for much higher salt precipitation than is in the initial residual brine, which is in line with field observations. Also, complete clogging of the near-wellbore formation would be possible (Miri et al., 2015, pp. 13–14).

2.3 Macroscopic salt distribution

According to Miri et al. (2015), local salt precipitation, which is a massive accumulation of salt at a stabilised drying front, occurs when due to the flow rate, the evaporation rate is much higher than the capillary backflow at the beginning (Miri et al., 2015, pp. 13–14). But as the drying front advances, the evaporation rate at the front declines (due to water vapour pressure increase), whereas the capillary backflow gradually increases (due to brine saturation gradient increase). Eventually, a steady state is reached, and the capillary backflow equalises the evaporation rate, and the precipitation front stabilises, (Miri and Hellevang, 2016; Ott et al., 2013). It is also important to observe that as a consequence of the strong capillary suction of formed salt, brine is continuously brought to the local precipitation area, but the evaporation may continue into the CO₂ phase inside the medium (Miri et al., 2015; Ott et al., 2011; Ott et al., 2013).

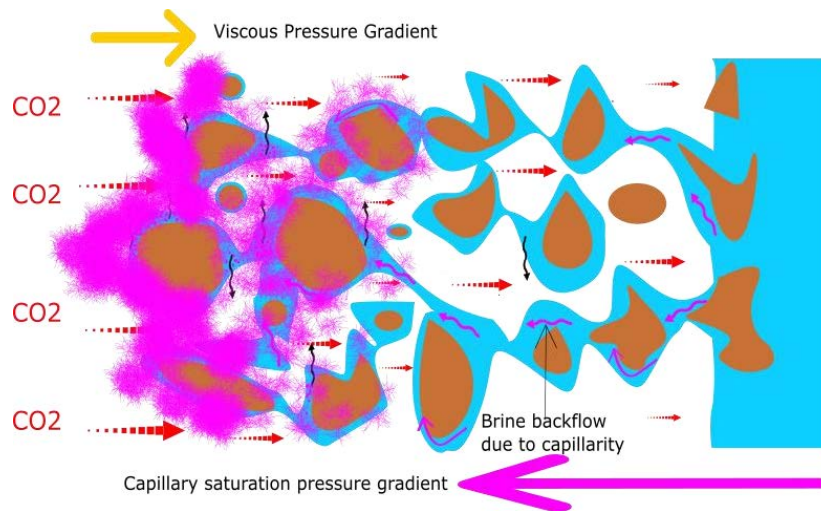


Figure 5: Visualization of a local salt precipitation due to a stabilized drying front. Brine is continuously brought to the salt drying zone causing more precipitation

A homogeneous salt distribution throughout the porous media is observed under two conditions:

1. Very low injection rates cause very low CO_2 velocity leading to very low evaporation rates. Drying causes a saturation gradient leading to a slightly equal capillary driven brine backflow. When the brine backflow at steady-state and the evaporation rate are equal, there is no formation of a drying/precipitation front. Continued CO_2 injection causes evaporation, salt diffuses into the aqueous phase leading to salt supersaturation and eventually drying throughout the porous medium (Miri et al., 2015; Ott et al., 2011; Ott et al., 2013; Ott et al., 2015; Ott et al., 2021).
2. When the CO_2 velocity is greater than the critical velocity limit at which the rate of evaporation is always greater than the rate of capillary backflow, regardless of the position of the drying front inside the porous medium (aquifer). The drying front will advance at a constant velocity inside the medium while immediately evaporating the trapped residual brine. The amount of salt precipitated depends on the concentration of salt in the trapped brine in pores and liquid films (Miri et al., 2015).

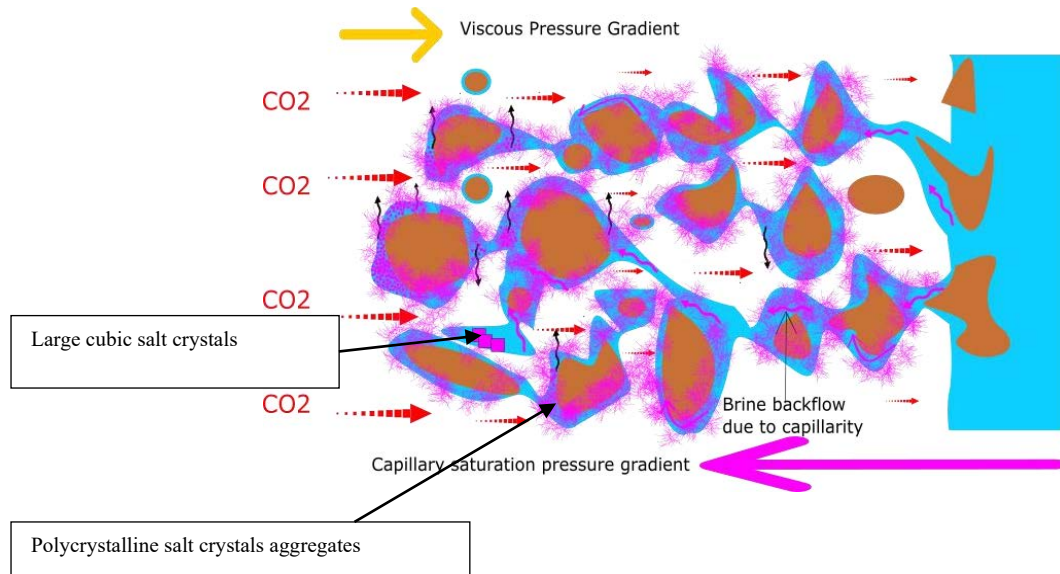


Figure 6: Visualization of the homogeneous salt precipitation. Salt precipitation is mostly where residual brine is located. CO_2 flow paths are left salt free

Because the effective flow paths of CO_2 are left barely occupied by salt, the homogeneous salt distribution model has shortfalls, according to Miri et al. (2015) (Miri et al., 2015). They claim that this model cannot explain the huge injectivity issues observed in the field. As already mentioned, the precipitated salt is very hydrophilic and has a strong capillary suction through a small layer of brine attaching it to the remaining brine films on pores. Therefore, brine is continuously sucked into the already formed salt, which makes salt precipitation much more than the experimentally restricted brine sample size (Miri and Hellevang, 2016, pp. 141–142).

2.4 Sensitivity analysis on the magnitude and distribution of precipitated salt

2.4.1 Magnitude

The progression of dry-out front and the magnitude of precipitation depends on several factors like CO_2 injection rate, temperature, pressure, fluid composition (salinity) and aquifer/formation properties like porosity, permeability, capillarity and heterogeneity (Pruess and Müller, 2009).

1. Salinity

The onset of precipitation depends on salinity, while also a higher salinity leads to increasing salt precipitation and, therefore, more porosity reduction. André et al. (2014) studies show that at high salinities, pores can get completely clogged, preventing any gas injection (André et al., 2014; Kim et al., 2012, p. 410) (André et al., 2014; Giorgis et al., 2007; Miri et al., 2015).

2. Injection Rate

Capillary backflow, according to some studies, is the reason for extensive salt accumulation. At high flow rates, such that viscous forces overcome capillary backflow, the intensity of salt precipitation is rebated. Attempts to define a critical velocity below which massive salt precipitation due to capillary backflow can be established have been made (André et al., 2014; Giorgis et al., 2007; Ott et al., 2015). However, no complete comprehensive model has been established yet.

3. Capillary Pressure

Although many studies have shown that capillary pressure increases the intensity of precipitation as it causes more fresh brine to backflow towards the drying front (Miri et al., 2015), some studies like Pruess and Müller et al. (2009) , perform numerical simulations which suggest capillarity has no significant influence to salt precipitation (Pruess and Müller, 2009). However, they suggest more experimental work is needed to understand capillary effects so that they can be accurately implemented in numerical simulations.

4. Aqueous Phase mobility

Increased brine mobility means less residual brine saturation at the drying front, thereby decreasing the intensity of salt precipitation. According to André et al. (2014), the amount of salt that precipitates during CO₂ injection heavily depends on the concentration of brine but also on the residual saturation of brine near the wellbore after the two-phase displacement by the gaseous CO₂ phase (André et al., 2014). When the residual saturation is low, limited precipitation is observed compared to when the residual saturation is high. According to Bacci et al. 2011, brine saturation depends on mobility (Bacci et al. 2011, p. 4450). When capillary pressure gradient due to the porous media petrophysical properties and also the formation of precipitates exceeds the viscous gradient (in the direction of CO₂ injection), brine with high mobility moves towards the injection point or salt front; a process that has been called capillary backflow in literature (André et al., 2014; Ott et al., 2011). More gas injection leads to further drying, and eventually, this increases the amount of precipitation far

more than what the initial residual brine contained. Hence a self-enhancing manner/mechanism (Bacci et al., 2013).

5. Temperature

Temperature effects are believed to be minimal. Nevertheless, high temperature induces an increase in the solubility of water into the CO₂ phase, and as a result, brine quickly reaches its saturation limit, and salt precipitation begins (Kim et al., 2012, pp. 413–414) (Miri and Hellevang, 2016, pp. 143–145).

2.4.2 Distribution

1. Injection rate

The injection rate factor is also discussed in section 2.3.

Kim et al. (2012) showed through 2D numerical numerical simulations that the injection rate not only affected the distance of the salt front into the formation but also the precipitation pattern (Kim et al., 2012, p. 410). They showed that at low injection rates, localised salt accumulation occurs. As the rate increases, salt accumulation tends to distribute more uniformly, and the salt front goes further into the formation.

André et al. (2014) explained two precipitation patterns observed in porous cores (André et al., 2014) . A non-homogeneous (localised salt precipitation) pattern where dissolved ions keep moving towards the evaporation surface or injection point because drying induces brine capillary backflow flow. On the other hand, a homogeneous pattern which simply means capillary backflow is not strong enough, and so a drying front continues to propagate into the formation. The strength of influence of the capillary backflow is governed by either the tightness of the porous media (low permeability and porosity) or by the strength of the viscous forces (CO₂ injection rate), whereby if the viscous forces are higher than capillary forces, a more homogeneous pattern tends to form. They predict a case-specific threshold value of the gas flow rate dependent on brine salinity beyond which the risk for clogging is low.

2. Temperature

Temperature differences cause density differences between the brine and CO₂, leading to the formation of the so-called CO₂ plumes, which leads to more localised salt precipitation at the dry out front. A more extended salt formation zone is observed (Kim et al., 2012).

3. Heterogeneity

According to Ott et al. (2014), microscopic heterogeneity in porous medium texture plays a fundamental role in controlling the evaporation of water, the exact location of salt deposits

and ultimately, the porosity and permeability relationship (Ott et al., 2014, pp. 8369–8370). They (including (Lehmann and Or, 2009; Nachshon et al., 2011; Ott et al., 2014, pp. 8369–8370)) find that in case a porous media where connected micro and macro-porous systems are in capillary equilibrium, evaporation from the micro-porous system is compensated by a capillary guided or induced flow from the macro-porous to the micro-porous system. This causes a high drying rate of the macro-porous system by flow, and as a consequence, salt precipitates in the micro-porosity while the macro-porous system permits gas permeability. However, Ott et al. (2013, 2014) show that active brine transport occurs from the microporosity to the macro-porosity (the CO₂ conducting pore volume which is first invaded) of a carbonate system leading to effective permeability reduction of CO₂ (Ott et al., 2013; Ott et al., 2014). According to Shokri & Or (2013), this solute transportation would also be observed if adjacent regions of the porous media had varying wettability (Shokri and Or, 2013).

2.5 Clogging modal and the Porosity-permeability relation

Change in pore volume due to salt deposition, growth or aggregation is properly captured by porosity. To be able to capture this change in pore morphology during the numerical simulation of salt precipitation, a clogging modal is needed (Masoudi et al., 2021). Clogging modals construe an inherent relationship between porosity and permeability changes (S. Parvin, M. Masoudi, A. Sundal, R.Miri, 2020). The choice of clogging modal depends on the mechanisms, processes, environment and materials as these can influence pore morphology change in different ways, while similar changes can cause completely different permeability changes. Therefore, regardless of the pore-scale processes, porosity changes and injectivity impairment will depend on the clogging modal used in the simulation. Hommel et al. (2018) compared different clogging models, their main characteristic features like degree of nonlinearity, threshold values like critical porosity and residual permeability of precipitate or biomass and their applications for biomass accumulation, mineral dissolution and precipitation. They note that the default clogging models for precipitation are the Power law variants, like the Verma-Pruess relation (Hommel et al., 2018). However, Parvin et al. (2020) and Masoudi et al. (2021) show that clogging models lead to massive errors in modelling permeability impairment during CO₂ storage, with different modals predicting huge differences in porosity for the same reduction in permeability (Masoudi et al., 2021; S. Parvin, M. Masoudi, A. Sundal, R.Miri, 2020). Also, a lot of clogging modals were constructed on a homogeneous layer of salt covering grain surfaces modal, including the

popular Verma-Pruess modal (Verma and Pruess, 1988). However, these modals can only capture the large single salt crystals that precipitate in the aqueous phase and probably do not capture the polycrystalline salt aggregates in the gas phase at the capillary and diffusive regime. Masoudi et al. (2021) developed a 3D pore-scale reactive transport modal to simulate polycrystalline salt aggregates and their effect on porosity and permeability and compared the modal with other clogging models. None of the known modals could simulate the polycrystalline salt aggregate hydraulic effects (Masoudi et al., 2021).

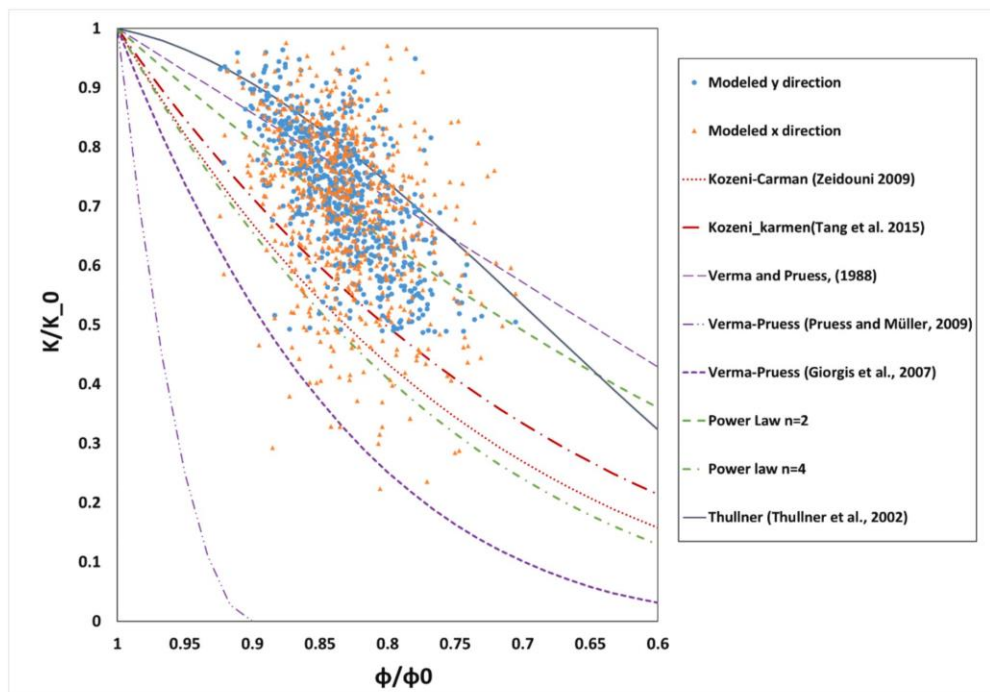


Figure 7: Showing a comparison between a derived modal for salt precipitation taking into account polycrystalline salt aggregates and other commonly known models. None of the models can closely predict the hydraulic characteristics change (Masoudi et al., 2021)

In addition, the Verma-Pruess modal (Pruess and Müller, 2009; Verma and Pruess, 1988), also known as the "tubes in series" modal, considers a porous medium as a succession of pores and throats, where the pores occupy a fraction of the connected path length (Bacci et al., 2011; Pruess and Müller, 2009; Verma and Pruess, 1988). The modal suggests that permeability may be reduced to zero at a finite porosity that corresponds to a fraction of the original porosity. Therefore, the modal is capable of predicting drastic unphysical permeability reductions corresponding to the local salt accumulation (Miri and Hellevang, 2016; Roels et al., 2016). Figure 7 for example shows that the verma-pruess modal

will predict no remaining permeability after a small change in porosity while the derived numerical of (Masoudi et al., 2021) fall way off this trend

2.6 The divergence in literature and the missing link

Much research has been done on salt precipitation in porous media, but there is no consensus on the right physical modal governing salt precipitation (Miri et al., 2015). Compounding the problem further is the obvious incontinences between results of similar experiments. For example, Miri et al. (2015) acknowledge this problem (Miri et al., 2015). They report that two similar experiments, one done by Ott et al. (2011) and another by Wang et al . (2009), give completely different findings (Ott et al., 2011; Y. Wang et al., 2009). Ott et al. (2011) observed that while absolute permeability decreased, effective CO₂ permeability increased five-fold, indicating a would be little or no change in CO₂ injectivity. They deducted that salt must have only precipitated in the areas previously occupied by the trapped brine, thus leaving the cross-section of the area of the percolation pathways open to CO₂ flux. On the contrary, Wang et al. (2009) found that the relative permeability to CO₂ was reduced by almost half (Y. Wang et al., 2009).

Miri et al. (2015) show that more salt can precipitate in the gas phase due to the surface energy-driven transport of salt water to the aggregate of growing salt (Miri et al. 2015). These aggregates would be able to completely cut off flow paths and cause injectivity decline assuming the salt is completely impermeable. Going by the modal explained above by Ott et al. (2011), a complete cut off of flow paths would never materialise (Miri et al., 2015, p. 11).

In addition to the current clogging models predicting unphysical salt precipitation mentioned in chapter 2.5. Miri et al. (2015) also suggest that most current salt precipitation models are insufficient. The models indicate that salt precipitation does not continue once grain-coating water films are completely vaporised (Miri et al., 2015). And at high flow rates, when viscous forces are higher than capillary forces, brine also does not flow back towards the drying front in the form of capillary backflow. This results in limited salt formation, which does not explain the considerable reduction in injectivity observed in the field. They suggest that there must be continuous feeding of brine to the drying front, which he explains by the hydrophilic nature of salt because of a thin brine film that continuously draws more fresh brine onto the already formed salt grains and aggregates (Ho and Tsai, 2020). This brine is continuously dried by CO₂ in a self-enhancing manner (Miri et al., 2015, p. 11) Because of all the ambiguities, a better understanding of the physical modal of salt precipitation is required.

2.7 Mitigation

Although there is still incomplete knowledge about salt precipitation or clogging physical mechanisms, some mitigation practices have been suggested.

The most common mitigation option is treatment with freshwater either as a pre-flush before CO₂ injection to decrease the salinity of near-well brine or flushing after clogging (Muller et al., 2009). However, fresh water is rather low in salinity and this can cause formation damage in presence of some clay minerals due to swelling. Formation damage and instability can also be caused by high mineral dissolution in the near well bore. Furthermore, injecting water-saturated CO₂ will lead to massive corrosion. Muller et al. (2009) also suggest saturation of CO₂ with water before injection. This is anticipated to reduce how much water evaporates into the CO₂ phase, hence reducing precipitation. Special care has to be taken for rock properties so as not to induce swelling due to freshwater injection.

According to Grude et al. (2014) and Hansen et al. (2013), low injectivity can significantly be overcome by injecting a mixture of methyl ethyl glycol (MEG) and water (Grude et al., 2014; Hansen et al., 2013). Also, high permeable material between the aquifer and the borehole along perforations is recommended (Kim et al., 2012; Miri and Hellevang, 2016, p. 145).

Chapter 3

Experimental Apparatus

In this chapter, I discuss the laboratory equipment and programs used to perform experiments and analysis of the results.

3.1 Apparatus

3.1.1 Microfluidics Devices

For a brief description of microfluidics devices, have a look at Mostafa (2017), Chapter 3.1. (Mostafa Borji).

3.1.1.1 Microfluidics Chips

Physical pore rock network EOR microfluidic chips from Micronit Lab-on-a-chip were used in these experiments. The chips are made of borosilicate glass which has a low thermal expansion coefficient making the chips resistant to thermal shocks.

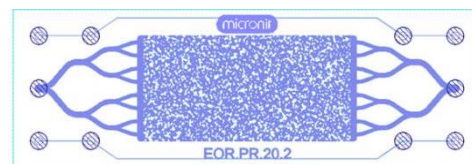


Figure 8: Visualization of the microfluidics model of a physical porous rock from a limestone sample, (MICRONIT, 2021)

Table 1: The dimensions of the physical network microchip (MICRONIT, 2021)

PROPERTY	DIMENSION AND UNIT
Porous medium length	20 mm
Porous medium width	10 mm
Channel height / Edging depth	20 μm
Total chip thickness	1800 μm
Bulk area	200 mm^2
Total grain area	75.4 mm^2
Areal porosity	0.62
Chip material	Borosilicate glass
Inlets	1
Outlets	1
Bulk volume	4 mm^3
Porous volume (PV)	2.4 mm^3
Volumetric Porosity	0.574
Permeability	2.5 Darcy

3.1.1.2 Chip Holders, connection setup and tubings

Due to the high-pressure-temperature conditions of the experiments, the high-pressure chip holder choice was made out of the available options. Steel tubings that can handle the acidic nature of CO_2 are used.

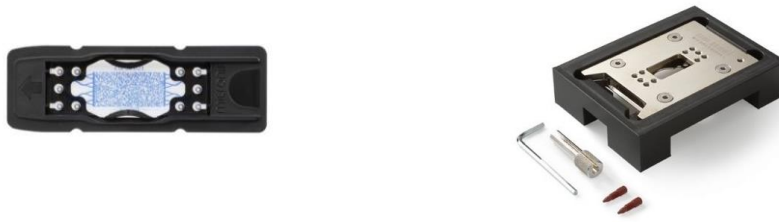


Figure 9: Showing a chip holder on the left and a high-pressure connection setup with fittings and ferrules on the right used in the experiments, (MICRONIT, 2021)

3.1.2 Microscopes

The Motic AE2000 microscope is used. It incorporates the colour corrected infinity optical system (CCIS) and inverted illumination using either Quartz Halogen or LED lighting for transmission and interchangeability (MOTIC). The observed images are transferred from the microscope to the computer monitor through a connection with a mounted camera. This camera, unfortunately, cannot provide a full range image of the micromodel in the microfluidics chip. This means an area in the observable view of the chip is selected and studied as the Region Of Interest (ROI). The microscope also has uneven illumination. Objectives available on the microscope include 2X, 4X, 10X and 40X.



Figure 10: The Motic AE2000 inverted microscope with a mounted digital camera and Monitor, (MOTIC)

3.1.3 Pump

The fusion 6000-X high-pressure syringe pump was used. The pump has a 700 lb linear pushing force, and it can be set for operation at a constant rate (0.0001mL/min to 408 mL/min) or a constant pressure with the add-on pressure sensor.



Figure 11: Image of the Chemyx fusion 6000 high-pressure pump, (CHEMYX, F. 6.-X.,

3.1.4 Syringes

The 6ml-volume chemyx stainless steel syringe with the high-pressure specification was used. Below is a specification of the chemyx stainless steel syringes.

SCALE VOLUME (ml)	INNER ID (mm)	MAX. PRESSURE (bar)	WEIGHT (lb)	Φ x LENGTH (mm)
6	9.53	150	0.36	13.5 x 167
10	12.60	110	0.5	17 x 167
20	19.13	50	1.0	23 x 167
50	28.60	20	1.34	33 x 167
100	34.90	10	2.0	39 x 189
200	43.96	5	3.30	49 x 206
300	54.00	5	4.19	59 x 206

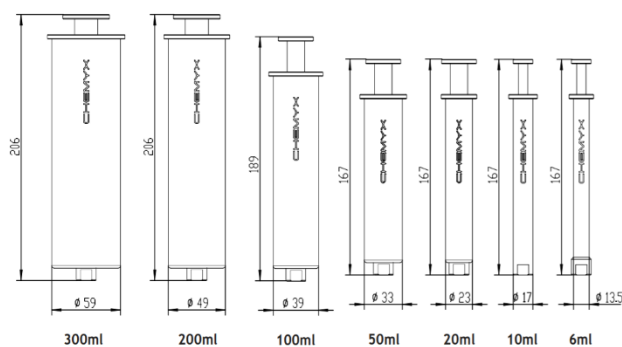


Figure 12: Chemyx stainless steel syringes specification, (CHEMYX, 2022)

3.1.5 Differential pressure transmitter

The Keller PD-33X differential pressure transmitter was used to measure pressure and pressure change across microchips for permeability calculations. An interface converter is used to relay measurements between device and computer. Using the Windows software Control Center Series30 (CCS30) program, pressure and temperature values and curves are measured, recorded and then later can be exported as a CSV file.



Figure 13: The keller pressure transducer, Series PRD-33X, (KELLER AG für Druckmesstechnik, 2021)

3.1.6 Backward pressure system

A back pressure system is set up against the injection direction to provide constant pressure conditions in the microchip so that supercritical CO₂ conditions are maintained. For the experiments done here, an Equilibar back pressure regulator was used with ratings of 6000psig inlet, 1500psig outlet, 0.05 maximum cv, and 150 °C temperature.



Figure 14: Equiibar back pressure regulator used in the experiments, (Fluid Controls Ltd, Dec 22)

3.1.7 Heating system

It was important to use a heating system to maintain temperature conditions for supercritical CO₂ in the microchip. The Leister Hot air blower with the mistral 6 system was used. The system is equipped with an integrated temperature probe, a display of target and current values, an automatic cool-down function, etc.



Figure 15: The Leister Hot air blower with the Mistral 6 system, (Leister Technologies AG, 2021)

3.1.8 ImageJ

The open-source java-based image editing and analysing software tool was used to study the results.

Chapter 4

Experimental setup, Procedure and Analysis

4.1 Preliminary Experiment

4.1.1 Setup and methods

Two Preliminary experiments were carried out. One of the experiments was to match the manufacturer's micromodel permeability. A multi-rate permeability experiment was conducted by injecting deionised water at different flow rates in the chip. Differential pressure was recorded using the CCS30 Windows software mentioned in Chapter 3.1.5. The stabilised steady-state pressure was read off as the rate pressure for each rate. Using Darcy's equation, the permeability k of the micromodel can be calculated (Whitaker, 1986).

$$q = \frac{Q}{A} = \frac{k}{\mu L} \Delta p$$

Where q is Darcy velocity (m/s), Q is flow rate (m³/s), A is area (m²), k is permeability (m²), μ is dynamic viscosity (Pa. s), Δp differential pressure (Pa) over Distance L (m)

$$Q = \frac{kA}{\mu L} \Delta p$$

A plot of Q against Δp gives a slope S from which the permeability k can be obtained.

$$S = \frac{kA}{\mu L}$$

Therefore,

$$k = \frac{S\mu L}{A}$$

The second preliminary experiment was done without inducing subsurface temperature and pressure conditions. Air was driven through a brine flooded micromodel using a vacuum

pump, and this air acted as the drying agent for the residual or irreducible brine in the micromodel. This preliminary experiment was meant to answer the concerns below.

- i) The pattern and manner of the salt precipitation
- ii) Does the salt formed in the microfluidics chips cover the entire depth of the chips? In some literature experiments, there is a suggestion that the formed salt could be a mere coating on the top and bottom of the microfluidic chips.
- iii) The above concern raises the question of the magnitude of porosity and permeability change caused by formed salt.

This preliminary experiment included injection and flooding of supersaturated salt-water solution (above 26% salt by mass) into the microfluidic chip. This flooding process ensured that no other phase remained in the chip apart from the brine. A vacuum was then applied to drive air through the microchip. At first, reducible brine is displaced, just like in the two-phase brine displacement by CO₂. After a while, irreducible brine remains, which then evaporates into the air being driven through the system by the vacuum. The result is the salt precipitation that forms throughout the chip in various patterns.

4.2 Primary Experiments

4.2.1 Experiment Design

Figure 16 below is the schematic of the equipment and materials used to perform the main parts of the experiments described in this thesis. The equipment and materials are described in 0.

The design consists of pressurised CO₂ and Nitrogen bottles. The Nitrogen is used to provide the backpressure needed in the system to keep CO₂ in a supercritical state. Backpressure of about 80 bar was used, and it is regulated by the Equilibar back pressure system as described in chapter 3.1.6. CO₂ is fed into the CO₂ pump through lines and valves three and four in the open position while valves one (the CO₂ relief valve), two, and five are closed. When pumping CO₂, valves three and six are in a closed position when four and five are in an open position. Valve seven is open or closed depending on whether vacuuming or pumping liquid respectively is going on. When pumping liquids like brine, distilled water and other cleaning liquids, the brine pump is used with valves five and seven in a closed position while the two-way valve six is in an open position.

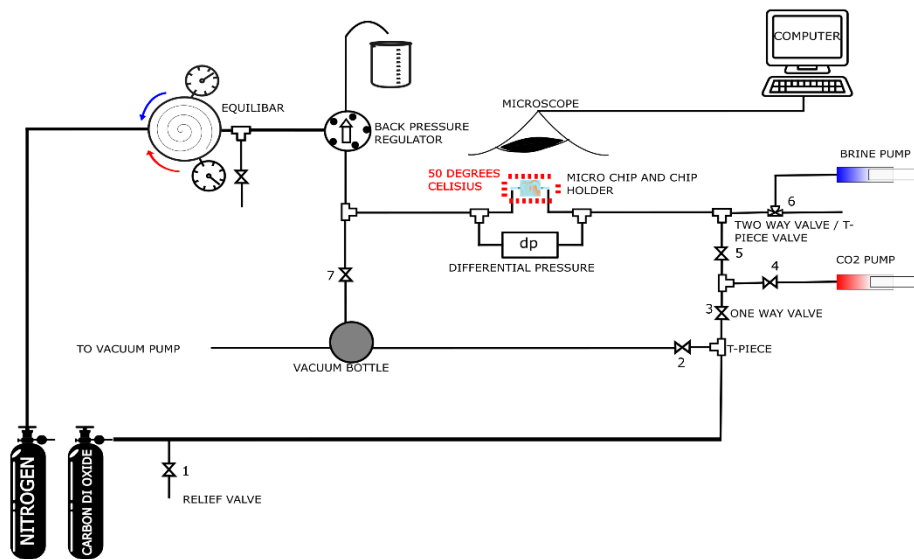


Figure 16: Showing the schematic setup of the experiments carried out

CO₂ and other fluids are injected through a micro model in the form of a microchip placed in a chip holder; see chapter 3.1.1. The backpressure is also the pressure condition expected to be in the microchip during injection, and in combination with heating, to about 50°C, supercritical conditions for CO₂ are obtained. The differential pressure across the microchip is measured by the pressure transducer connected to either end of the microchip. The pressure measured is also logged and saved at customised time steps. The microscope is used to either take timestep images of the microchip or live video. The pressure logs and images are saved on the computer for further analysis.

4.2.2 Experiment procedure

4.2.2.1 Step 1: Multi-rate permeability k with liquid CO₂

After filling the CO₂ syringe and getting ready to pump liquid CO₂ to the microchip, two physical conditions should be considered. The first is that the CO₂ is at about 57 bars of pressure. Opening the valve to start injection into the microchip without any back pressure in the system means introducing a substantially higher pressure from the CO₂ to the rest of the system. This CO₂ pressure will push and bypass everything through the micromodel without control to the outlet where it is immediately a gas. Secondly, if the flow lines connecting the CO₂ syringe to the micromodel are empty and under pressure (lower than 57 bar), the liquid

CO₂ will instantly expand and become gas.

The following is done to ensure that there will not be CO₂ expansion and substantially lower pressure in the system when liquid CO₂ injection starts. Flood the flow lines and the microchip with distilled water at the experimental backpressure of about 80bars, as explained in chapter 4.2.2.2 below. This ensures that the flow lines are not empty and contain fluid at a substantially higher pressure than the incoming CO₂. In this case, no bypass and instant gasification occur.

Liquid CO₂ is then injected at three or four different flow rates while pressure is being measured. At each rate, pressure is monitored until a steady state is reached and maintained for a substantial time before changing to the next flow rate. The permeability is then calculated, as is explained in the preliminary experiment using distilled water. See chapters 4.1.1, and 5.1.1.

4.2.2.2 Step 2: CO₂ injection in saline micro model

Three brine solutions were prepared using deionised water (DI) and Sodium Chloride (NaCl). The solutions prepared contained 20%, 10% and 5% NaCl by mass, or 20,000ppm, 10,000ppm and 5,000ppm respectively.

The entire system was then vacuumed, from the brine syringe to the vacuum bottle through the microchip. Also, the line from the CO₂ syringe and CO₂ relief valve (valve one in Figure 16) to the vacuum bottle is vacuumed. After the brine syringe is filled and mounted, care is taken that no air is injected into the system by first producing a few millilitres outside the system using the two-way valve six in Figure 16. The microchip is then completely flooded with brine. The liquid CO₂ is injected with a back pressure of 80 bars. The brine must be injected with the same backpressure to ensure that when the CO₂ line is opened, it is opened to the 80bars pressured system. Otherwise, the system would have a low pressure of a few psi gained during brine flooding, yet liquid CO₂ carries with it 57bars. CO₂ fills the syringe with the pressure of the storage bottle of about 57 bars. The high-pressure difference would cause rapid CO₂ expansion when valves four and five are opened for CO₂ injection. The combination of expansion and the 57 bars of pressure causes the CO₂ to bypass everything, including the dead brine volume in the lines, and run through the chip immediately to the backpressure system where the pressure is higher than 57 bars.

After correctly flooding with brine, with the back pressure of 80bars and temperature fixed to about 50 °C, CO₂ is injected. CO₂ was injected at 0.2ml/hr, a rate where at least 2000 Pore Volumes (PV) are injected every 24 hours.

Injecting CO_2 at the mentioned temperature and pressure conditions ensures that the liquid CO_2 from the bottle is dry supercritical CO_2 when it reaches the microchip. CO_2 is supercritical at 31°C and 73 bars. However, slightly higher pressure is chosen to be well within the Supercritical region. A higher temperature is selected because of temperature losses due to the circulation of air around the chip. The desired path to the supercritical state in the microchip is shown in Figure 17 below. It is essential to avoid going through the gaseous phase.

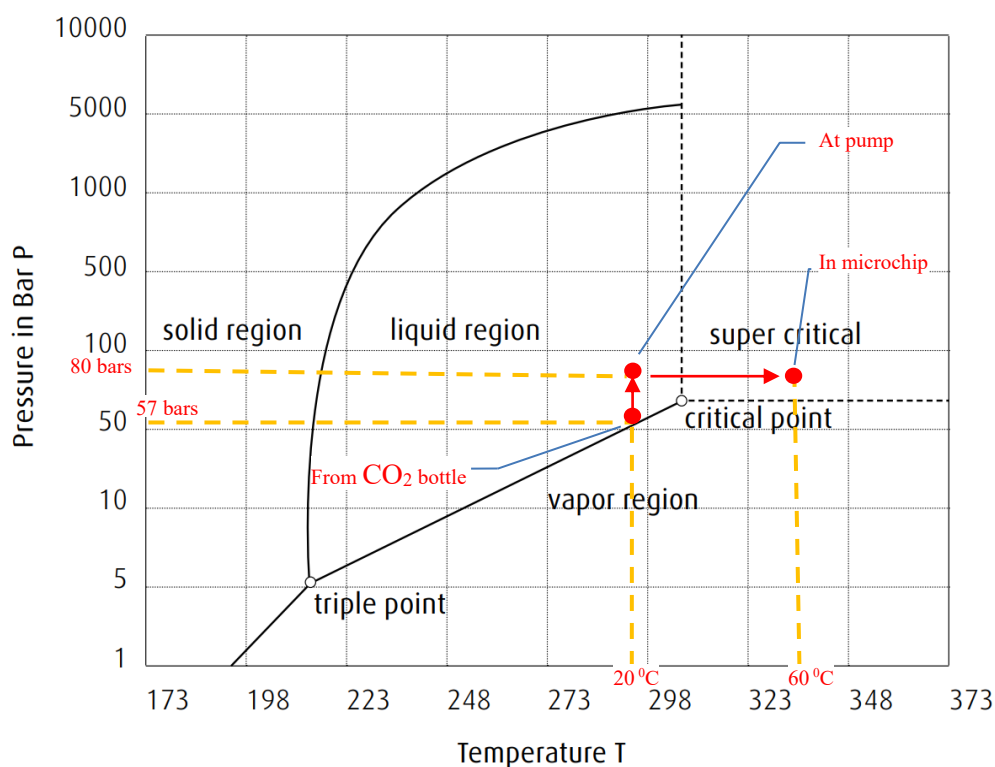


Figure 17: Showing the desired path from liquid CO_2 in the bottle to Supercritical CO_2 in the microchip

During CO₂ injection, the pressure is measured by the transducer and logged by the software. Salt is visualised by the Motic AE2000 microscope (0), and a series of images for a randomly chosen area of the microchip are taken at 5 minutes intervals. The area will be hereon referred to as the Area Of Interest (AOI) shown in Figure 18. CO₂ injection is continued until the microchip is completely dry.

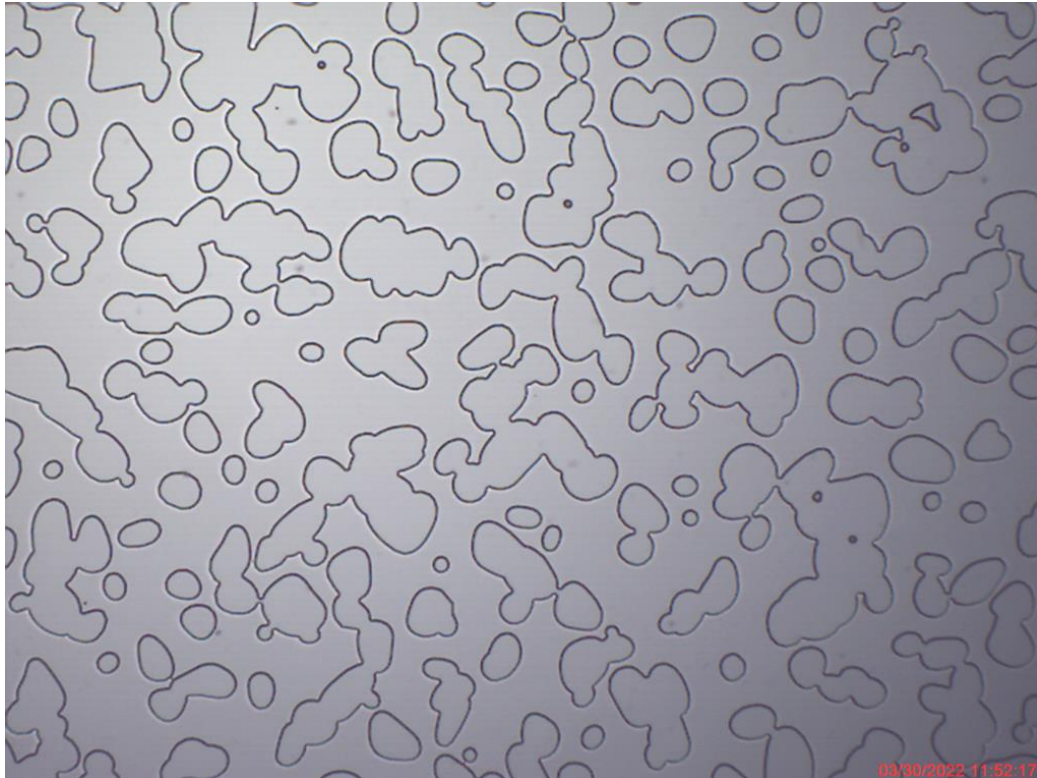


Figure 18: Showing the mage of the Area Of Interest for the main experiment

4.2.2.3 Step 3: Multi-rate permeability k of a microchip with precipitated salt using liquid CO₂

After salt precipitation for the three different brines, the next step is to investigate the change in permeability of the micromodel. As done in chapter 4.2.2.1 above, three to four different flow rates of liquid CO₂ are used to calculate multi-rate permeability.

4.2.2.4 Step 4 Investigation of the effect of salinity

Clean the microchip as described below in chapter 4.2.3 and repeat Steps 2 and 3 for the different brine salinities.

4.2.3 Procedure for Cleaning Microchip

The entire system is vacuumed for about 5 hours to ensure all fluids in the flow lines are reduced to as little as possible, even the liquid to the flow lines connecting the

transducer. Then distilled water is injected to dissolve the salt formed in the microchip and that which may have formed in the flow lines. About 10 to 20 ml at a low flow rate for about 24 hours is optimal.

If there is some colouration and aggressive stains in the microchip, probably due to metals being mobilised as a result of corrosion or rusting, another cleaning procedure should be taken. The backpressure of the system is turned off to enable the injection of cleaning fluids at higher rates. Then vacuuming is done for a substantial time. Injection of distilled water 6-10 ml at a high rate, probably 10ml/hr. If there is little to no change, distilled water alone will not clean the micro model. Injection of 6-10 ml of diluted Hellmanex is an option. Hellmanex is a special glass, Quartz, and optical parts alkaline cleaning concentrate. It is composed of wetting agents, emulsifiers, Ampholytic agents, surface-active agents, complexing agents and potassium phosphate. It removes dirt particles while its emulsifying and dispersing abilities prevent the redeposition of loosened particles (Hellma, Registered Trademark, 2022). After Hellmanex is injected, distilled water is injected, 10-20 ml at 10ml/hr.

If the microchip is still not clean after this stage, inject 10-20 ml of diluted Hydrogen peroxide (10% by volume), a bleaching agent. Inject distilled water 10 to 20 ml for about 24 hours. If complete cleanup is not achieved, inject distilled water for a longer time and if there is little to no change, with lower injection rates, repeat steps from the injection of Hellmanex. Care should be taken not to inject Hellmanex for extended periods (longer than 2 hours).

Chapter 5

Results and Discussion

5.1 Preliminary Experiments Results and Discussion

5.1.1 Multi-rate Permeability k of the Microchip with Water

Table 2: Showing the summary of data used to calculate the permeability of the microchip when distilled water is the working fluid

Rate, ml/ hr	Rate, m3/s	delta, psi	delta P, pascals		
0.1	2.78E-11	0.202	1399		
0.5	1.39E-10	0.893	6161		
1	2.78E-10	1.724	11886		
5	1.39E-09	6.991	48201		
10	2.78E-09	14.028	96719		
		Units			
Area, Edging depth* Width	0.0000002	m ²			
viscosity water @25°C	0.00089	Pa. S			
length, L	0.02	m			
Slope	2.91554E-14				
k, m ²	2.59483E-12	m ²		Manufacture's k	D
k, D	2.6	Darcy		2.5	Darcy
k, mD	2647	mD			

A steady-state pressure was obtained for each rate by injecting distilled water at different rates (at least three stable rates), as shown in Table 2 above. The rates and pressure were used to calculate the permeability of the microchip. Permeability of 2.6 Darcy was obtained, which is close to the manufacturer's permeability of 2.5 Darcy. The difference could be due to differences in pressure measurement sensitivity.

5.1.2 Salt precipitation

Driving air through a brine flooded microchip achieved the two-phase displacement of brine by air, evaporation of brine into the air and eventually total dry out in the microchip.

5.1.3 Nature of salt precipitation and patterns

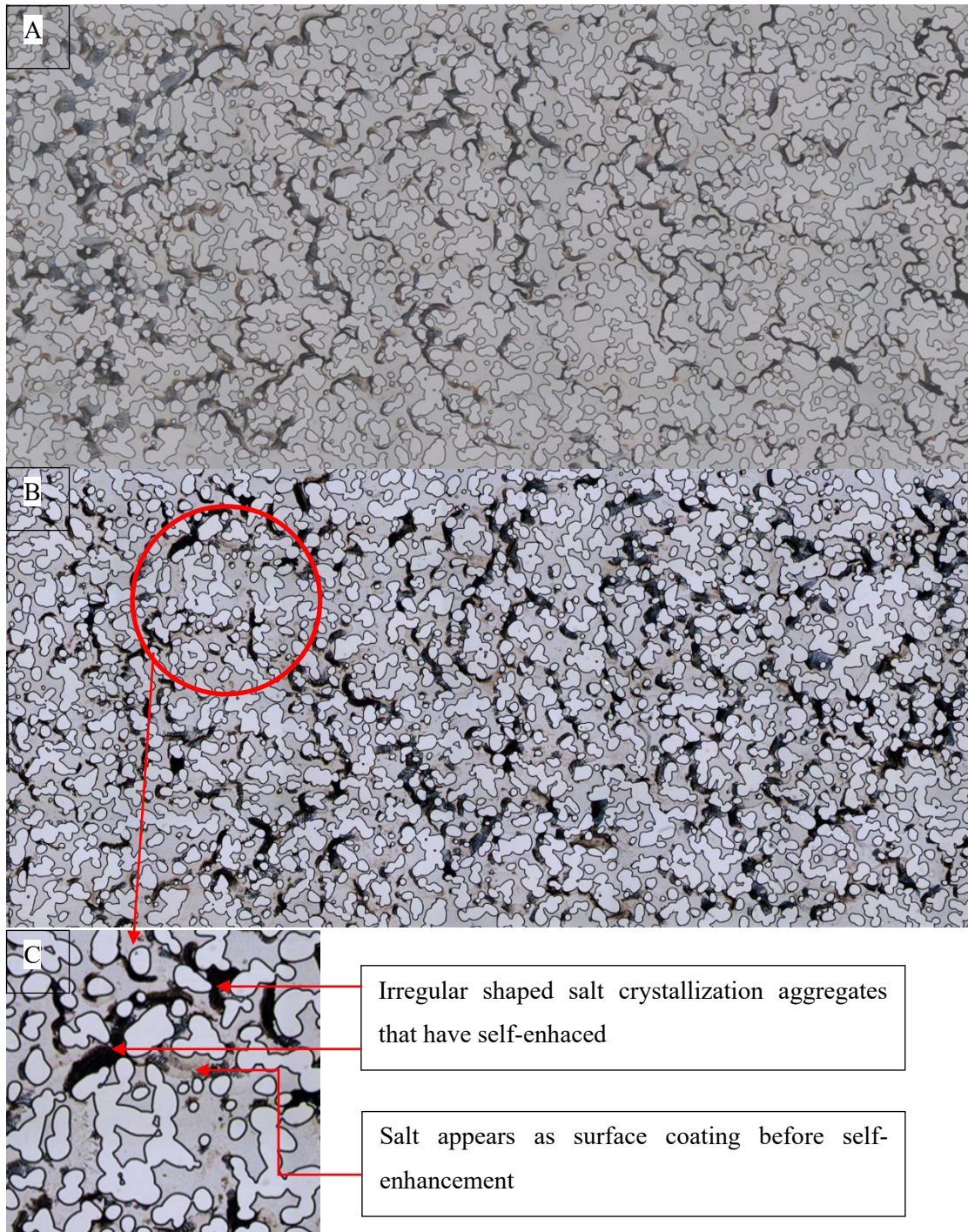


Figure 19: Images of Microchip with polycrystalline salt precipitation as irregular random patterns, A and B. Also shown is the crystallization before self-enhancement, C.

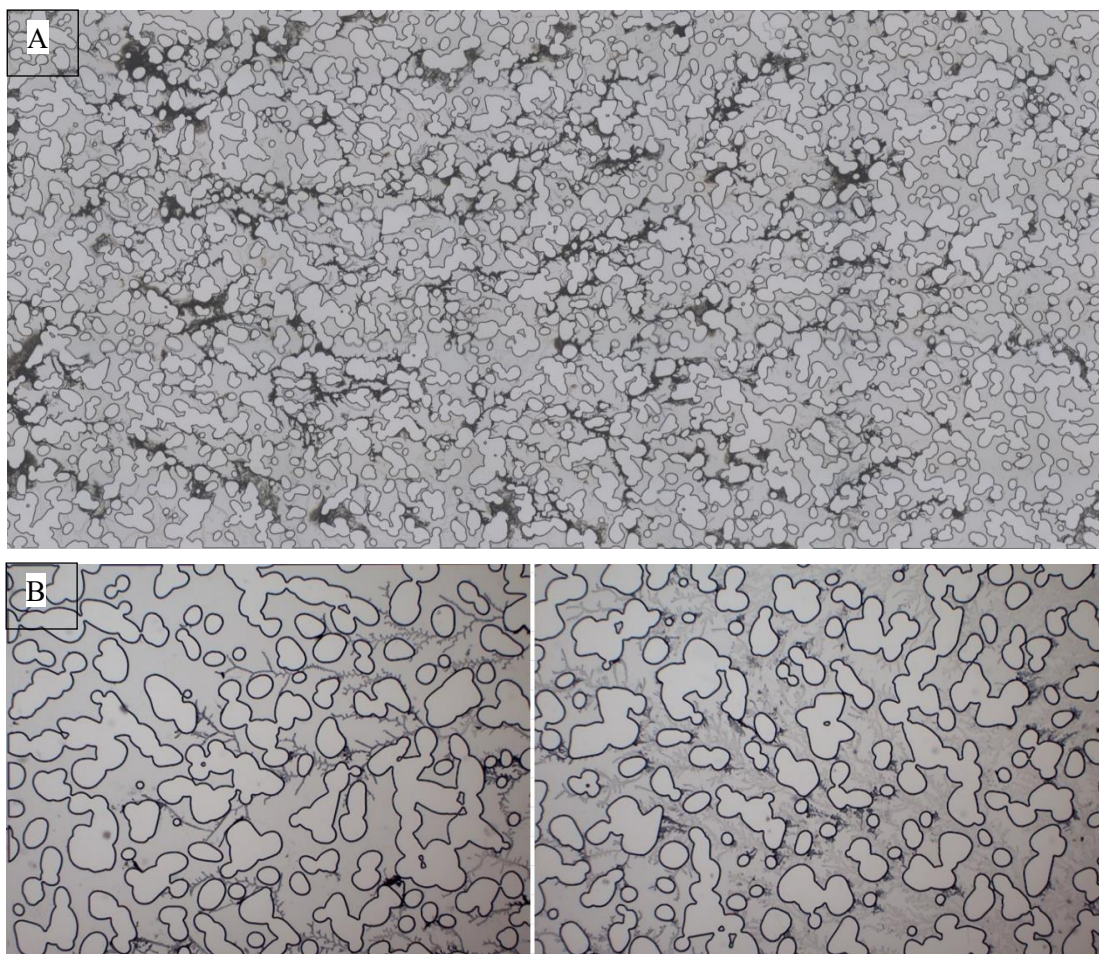


Figure 20: Showing Dendritic shape patterns of the polycrystalline salt.

Polycrystalline salt precipitated in two main patterns: irregularly shaped aggregates and dendritic shaped salt aggregates. At very few locations, salt also precipitated as large cubic crystals. Images in Figure 19 and Figure 20A show patterns that were obtained with supersaturated brine, while the image in Figure 20C was obtained when very dilute brine was used (5% brine by mass volume). The difference in the patterns when supersaturated brine was used could be related to the velocity of air in the microchip. Although the same vacuum pump was used to drive air through the microchips at the same rate, sometimes salt blockages at the inlet caused air velocity to vary.

Polycrystalline salt precipitation was observed to occur in the drying phase (air or gas), while cubic crystals occasionally formed in the brine phase, where there was enough time for complex crystallisation.

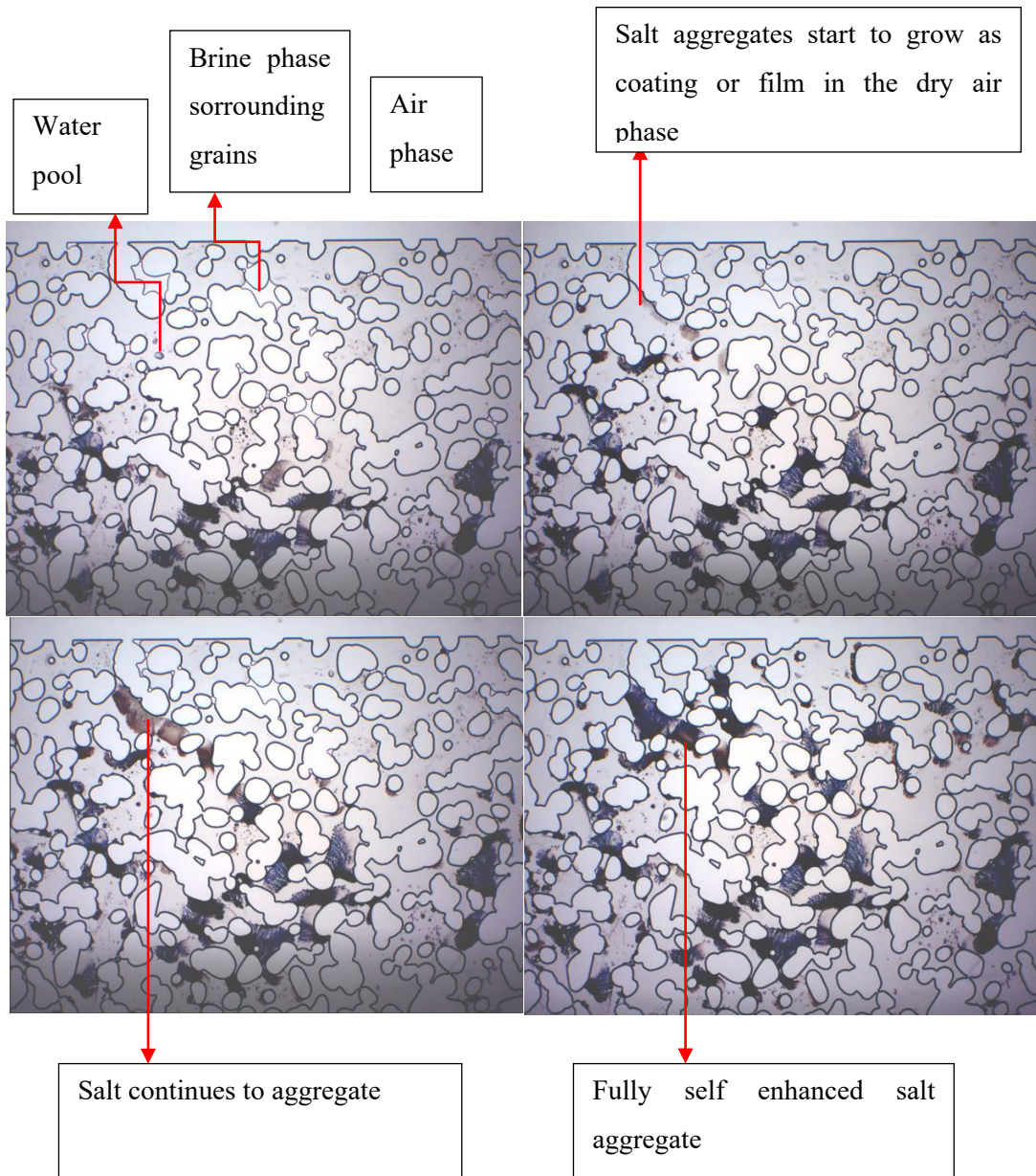


Figure 21: Showing the growth of random shaped salt polycrystalline aggregates in the dry air phase

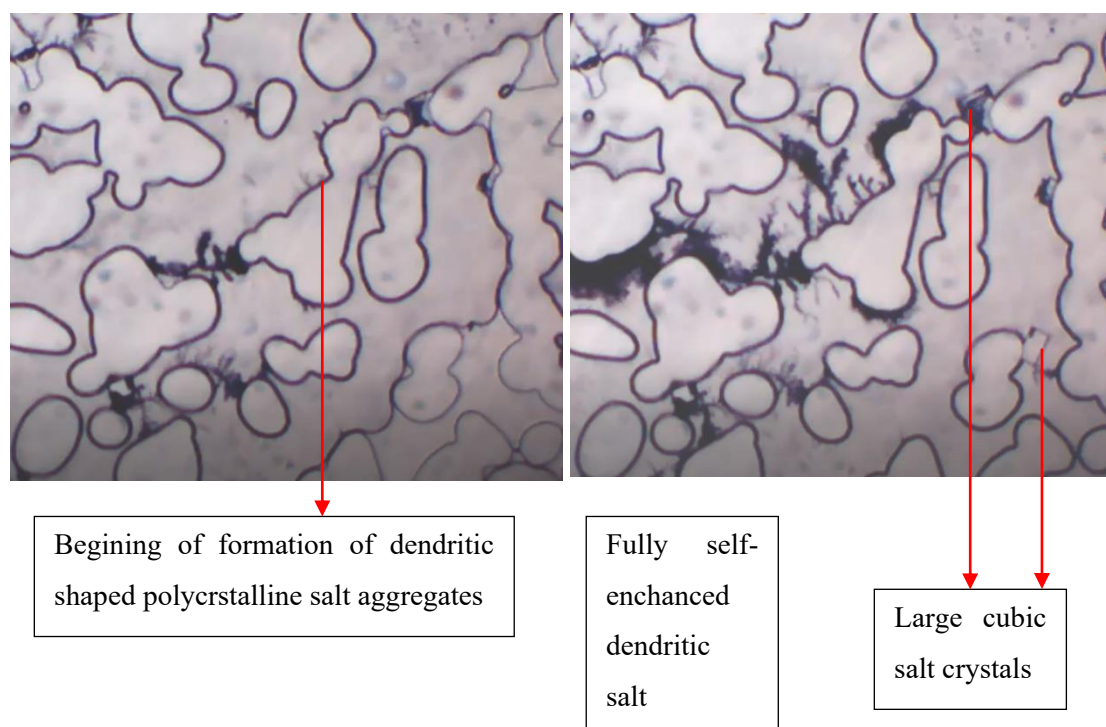


Figure 22: Images showing the growth and development of dendritic shaped salt aggregates and large cubic salt crystals

5.1.3.1 Depth of coverage of salt in the microfluidic chip

The microfluidics chip with the precipitated salt was put under the Motic AE2000 inverted microscope in the X10 objective. The focus was changed such that the top of the microchip was the most sharpened view, and at this point, there is no sharpness on any of the precipitated salt because the salt is within the edging depth of the microfluidics chip. The focus was then slowly changed until the sharp view of the precipitated salt just under the top end of the microchip glass was observed. At this point, the microscope's focus is at the top of the microfluidics edging depth. The process was continued, transferring the microscope's focus from top to bottom into the microchip until the bottom while observing the sharpness of the precipitated salt. Beyond the microchip's bottom end, all focus on the precipitated salt is lost. A change in the sharpness of the salt aggregate in the chip from top to bottom means that salt aggregate does not cover the entire depth of the microfluidic chip. The observation made is that for some, the sharpness changed to various crystals as these crystals are believed to be arranged randomly, some on top of each other through the edging depth. For the very light-coloured salt (coating-like), the sharpness faded within the focus depth of the chip. Salt occupied the entire edging depth for the very dark massive aggregates. Hence salt precipitated as a coating on the top and bottom of the microchip, as massive aggregates filled the entire edging depth in some places; see Figure 23 below.

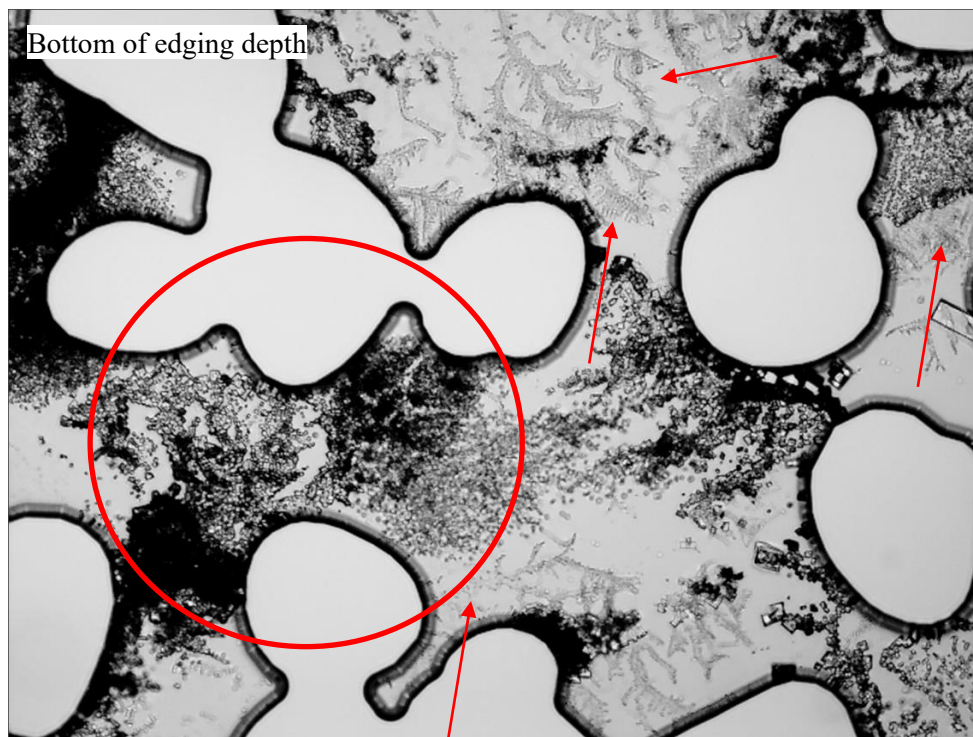
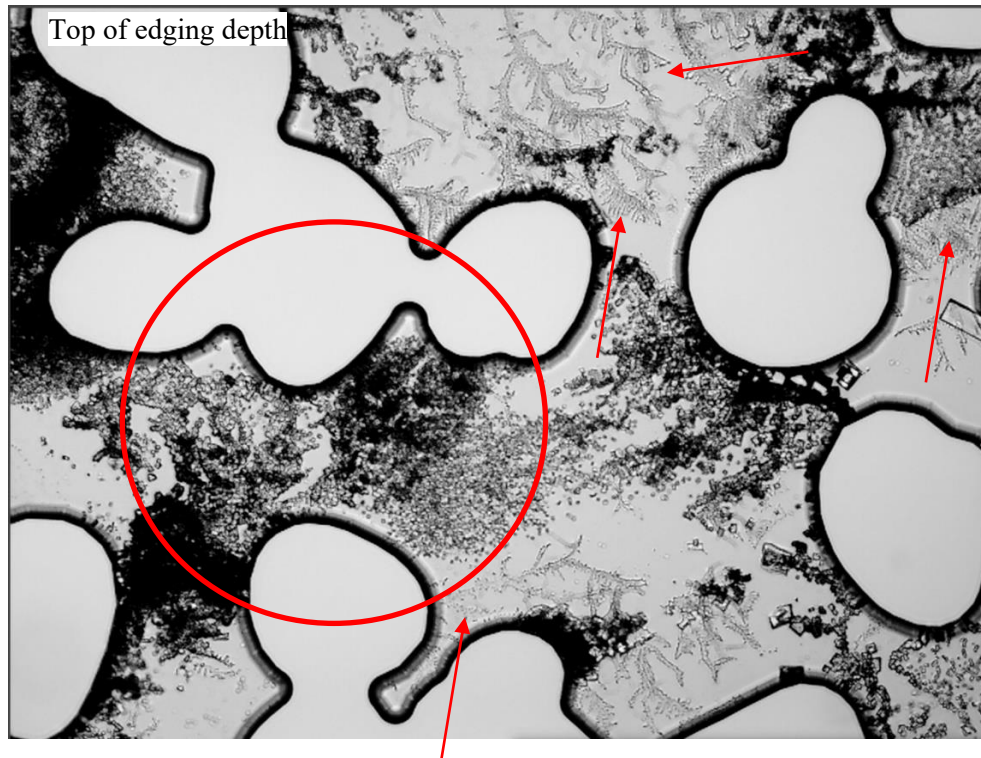


Figure 23: Showing the microscope focus at the top and bottom of the microfluidics edging depth. The precipitation that shows a change in sharpness from top to bottom is indicated by the red arrows and the precipitation that does not cover the entire microfluidics chip edging depth. The aggregates, for example in the red circle, are salt crystals crammed together and occupying different vertical positions. Sharpness changes for various crystals. The very dark aggregates occupy the entire edging depth

5.1.4 Porosity change analysis with Fiji ImageJ

After identifying which part of the precipitate occupies the entire porous medium depth, it is important to estimate how much of the porosity is reduced by the salt precipitation. Using Fiji ImageJ software, images of the clean chip before salt precipitation and of the chip with precipitated salt were uploaded into the software, processed, and analysed. The salt precipitated image is turned into 8bit images and while the clean salt-free image is turned into a binary mask for comparison analysis.

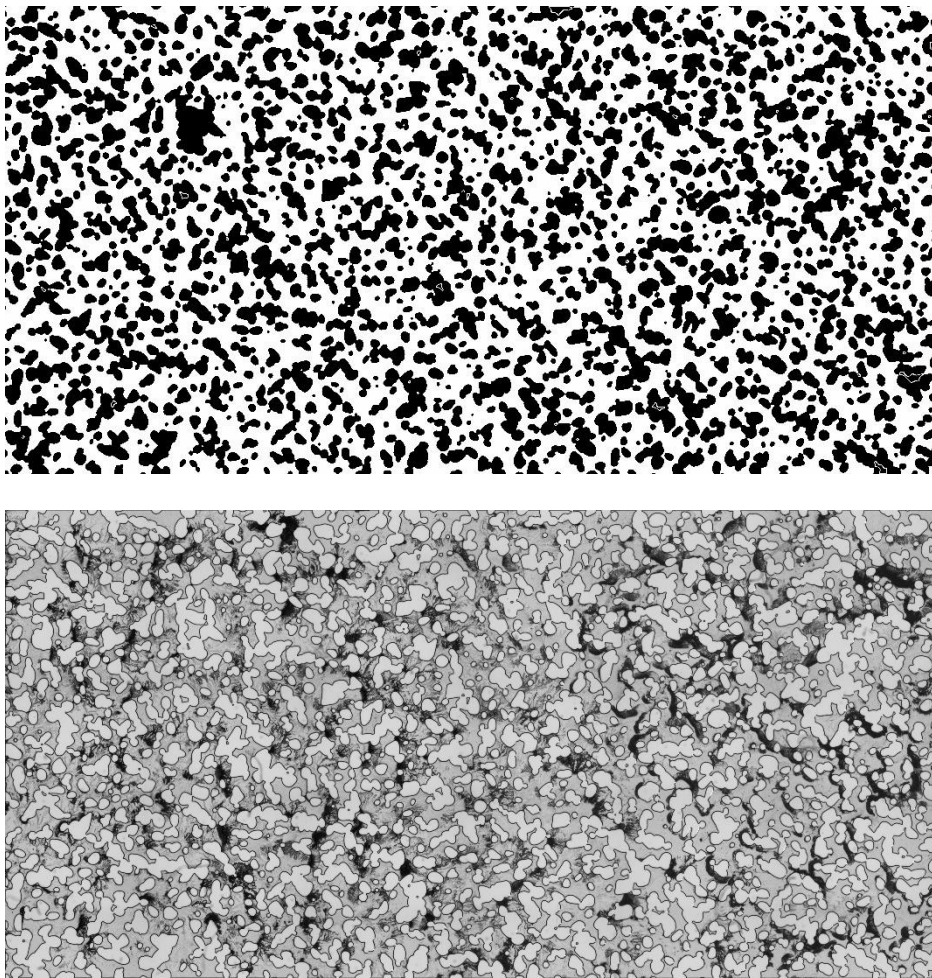
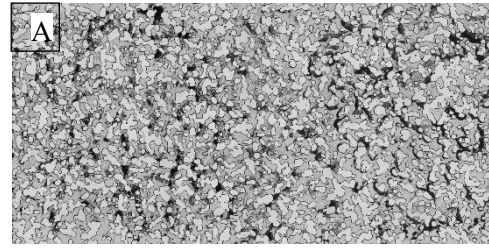


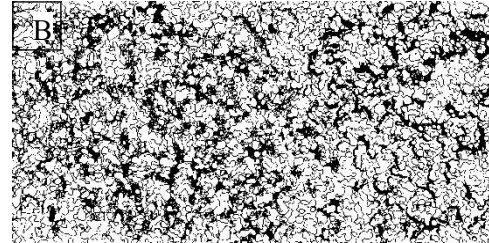
Figure 24: Showing at the top the mask of the salt-free image, and the salt precipitated image at the bottom

Using the Threshold calculator under image tab in imageJ, the salt with the very light colour is eliminated from the salt image; see Figure 25 below. ImageJ is capable of showing the grey value on every point of an image. To know the grey value of a point in the image, the cursor is hovered over the point of interest, and the value is displayed at the bottom of ImageJ's tool panel. The values fall within 255 for the darkest colour (black) and 0 for the lightest colour (white).

A: 8-bit image of chip with precipitated salt



B: Image A with 35% of the lighter shades of grey. Threshold cut-off value at 167



C: Image A with 25% of the lighter shades of grey. Threshold cut-off value at 192

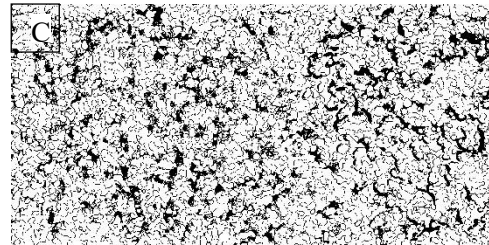


Figure 25: Showing the representation of the salt at different Threshold cut off values.

The light greys representing the salt that does not cover the entire edging depth is eliminated in Image C

The next step is to use ImageJ's Image calculator under the processes tab to "Add" the clean salt-free image with the precipitated salt image, part A Figure 26. An 8-bit image is obtained, which is then transformed into a binary image of just black and white, B and C Figure 26. Using the Threshold calculator again, the cut-off values of Image C in Figure 25 are applied to the results image to remove the salt that does not cover the entire edging depth of the microfluidics chip.

Then using the image, the measurement process under the analyse tab, the area that is covered by the grains and the salt is calculated for both the salt-free chip and that with precipitated salt. The results are summarised in the table below. The results show a 21% decrease in porosity of the microfluidics chip due to salt precipitation.

The next step is to measure the decrease in permeability. Multi-rate permeability experiments can be done with supersaturated brine (this would not dissolve any of the salt). However, the salt was always displaced even at very low injection rates. Multi-rate permeability shall be done with liquid CO₂ in the primary experiments.

Table 3: Showing the porosity of a fresh, clean microchip and that of a microchip after salt precipitation

Percentage areas of chip elements		
	Clean chip	Chip with salt
Grains	40%	40%
Grains + salt	40%	61%
Porosity	60%	39%

Initial chip with 60% porosity

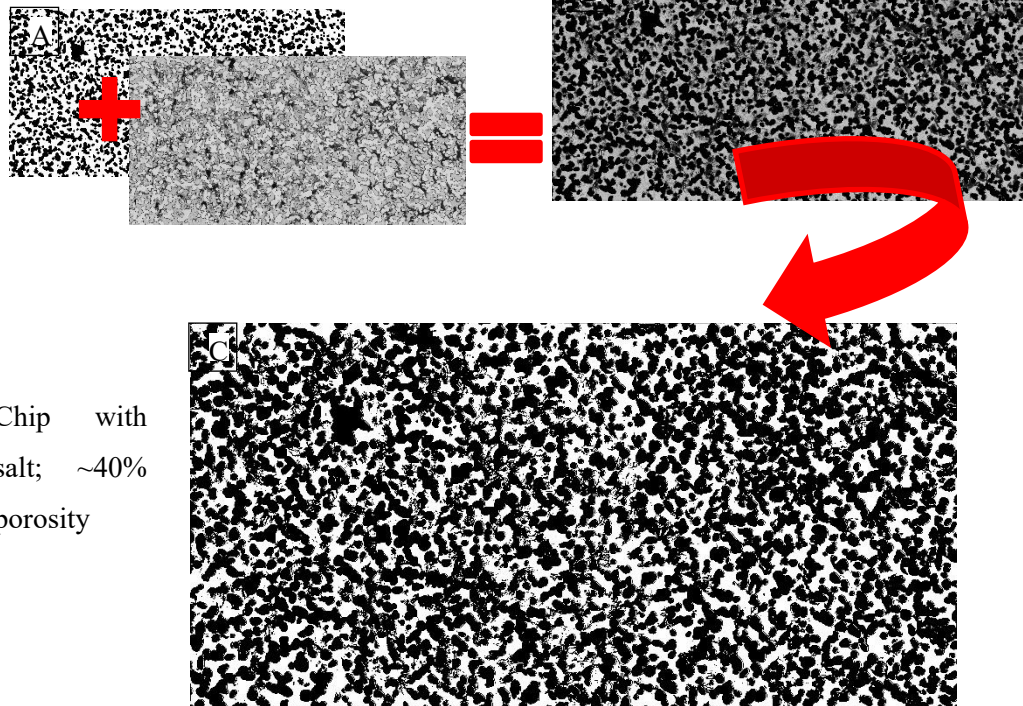
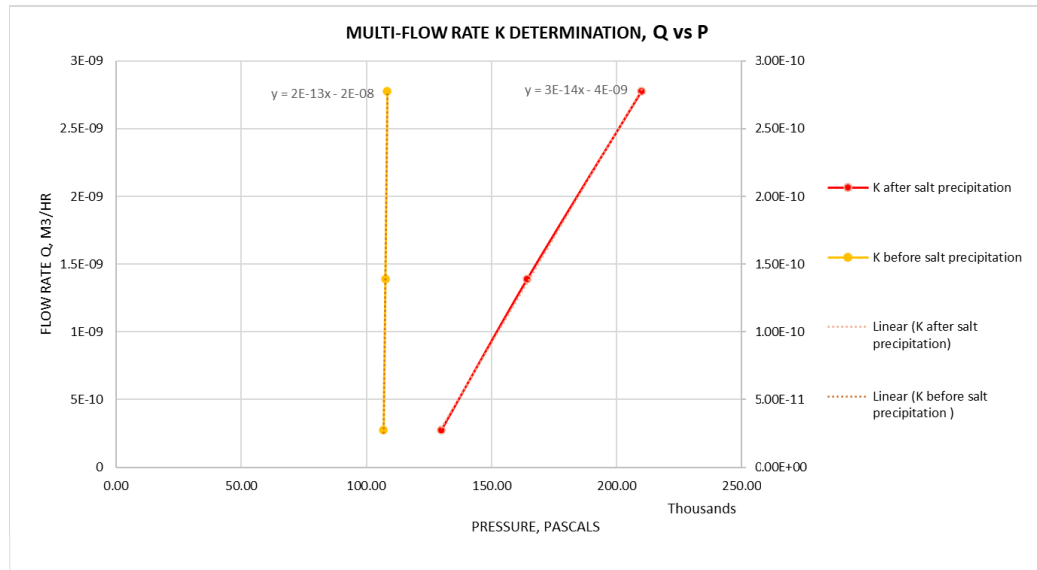


Figure 26: Showing the added images A, the resulting 8-bit image B, and finally the binary image C after applying appropriate cut off values in the Threshold. The porosity decreased from 60% to 39%, a 65% decrease in porosity due to salt precipitation.

5.1.5 Permeability change using multi-rate flow rates with air

Three flow rates of 0.1, 0.5 and 1 ml/hr of air were injected into a clean microchip and the permeability was calculated using the Darcy equation as illustrated in section 4.1.1. After salt precipitation, the same experiment was repeated with flow rates of 1, 5, and 10 ml/hr and permeability was calculated again. Results indicated a reduction in permeability of almost 80% for a 20% porosity reduction as seen in the previous section. The pressure difference response from the clean chip (before salt precipitation) was very low due to the very low rates used.



permeability of the clean and salt-precipitated microchip

The graph shows a higher slope for the clean chip meaning permeability declined when salt precipitated.

5.2 Main Experiment Results and Discussion

5.2.1 Multi-rate Permeability k of the microchip with liquid CO₂

Table 4: Showing the summary of data used to calculate the permeability of the microchip when liquid CO₂ is the working fluid

Rate, ml/ hr	Rate, m3/s	delta, psi	delta P, pascals		
0.1	2.77778E-11	0.3	2068		
1	2.77778E-10	1.8	12410		
2	5.55556E-10	3.3	22752		
		Units			
Area, Edging depth*Width	0.0000002	m ²			
viscosity water @25°C	0.00089	Pa. S			
length, L	0.02	m			
Slope	2.5515E-14				
k, m ²	2.27E-12	M ²		Manufacture's k	D
k, D	2.32	Darcy		2.5	Darcy
k, mD	2317	mD			

It is essential to estimate the permeability of the microchip using liquid CO₂ as the working fluid because liquid CO₂ is the intended fluid to be used calculate the permeability impairment after salt precipitation. Water cannot be used as it would dissolve the salt. Three stable injection rates at steady-state pressure were used to calculate permeability. Although the injection rates differed from those used with distilled water as the working fluid, the permeability obtained is quite close. The similarities in permeabilities are probably because the difference in the densities of liquid CO₂ and water is slight.

5.2.2 Salt precipitation in the micro model (Microchip)

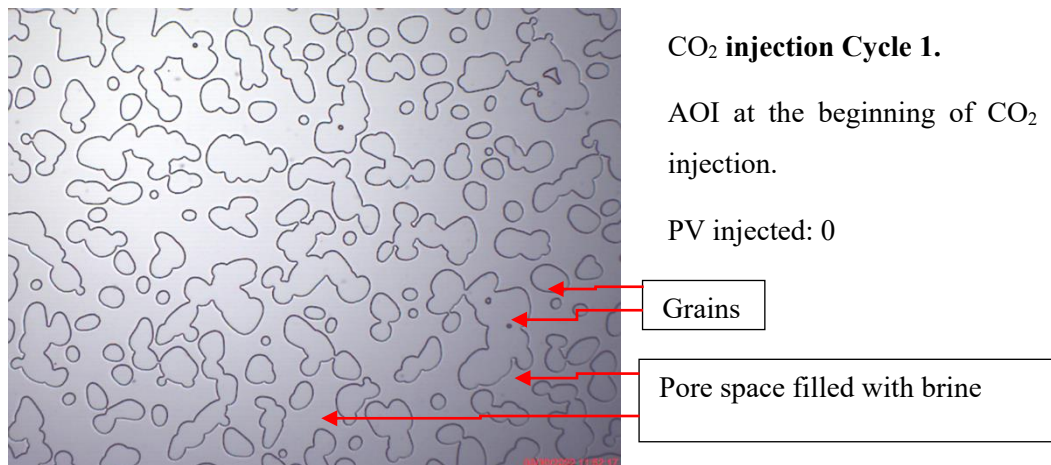
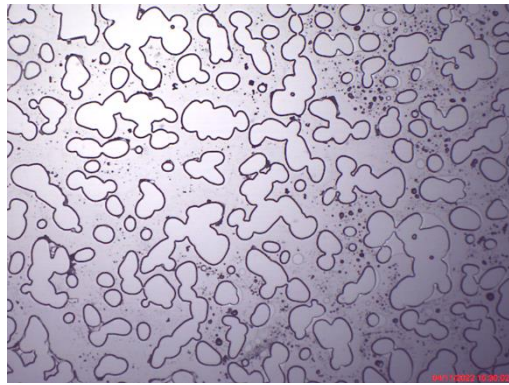


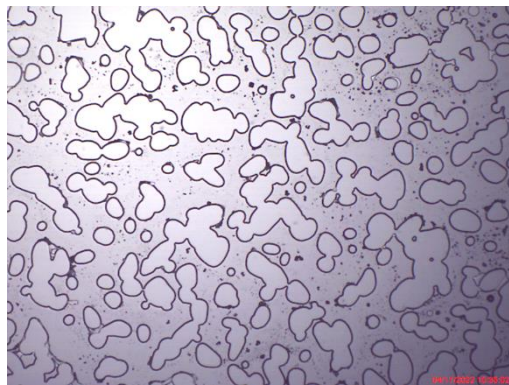
Figure 28: AOI at beginning of CO₂ injection cycles after Brine flooding

After flooding the microchip with brine, CO₂ injection was started. Figure 28 above shows the status of the microchip just before CO₂ injection. CO₂ injection was done with a 6 ml syringe, and this required multiple refill cycles. The microchip achieved complete dry-out and salt precipitation after 13 cycles and 23,456 pore volumes. However, due to technical issues like brine backflow, it is assumed that complete dry-out should have been achieved much earlier. Figure 29 below shows the status of the microchip after 13 cycles. The amount of precipitated salt was far lower than expected and not even close to that which was achieved in the preliminary experiments. Due to technical issues, there was a CO₂ rush into the microchip after the start of the CO₂ refill cycles. This washed residual brine from the microchip, thereby reducing the amount of precipitation that would have occurred.



25 hours after cycle 12

Continued drying of residual Brine



CO₂ Injection Cycle 13.

At refill and restart: No observed immediate changes and gas rush. Refill-restart procedure slightly changed

PV Injected: 23,456

Figure 29:AOI at the End of the experiment. Complete dry out, 23,456PV injected

The results of this experiment were hugely affected by the unreliable refill-start procedure that caused the inflow or backflow of brine back into the micro chip and also the rush of CO₂ into the chip.

A rush of CO₂ into the lines and microchip, immediately washed away brine and CO₂ from the microchip. The result was a complete change of status in the chip and, therefore, a lack of steady control of two-phase displacement and drying processes. This problem could have arisen from the fact that the CO₂ syringe plunger was first withdrawn with valves three, four and five closed during refill. This procedure creates a situation where the volume in the CO₂ syringe increases, causing pressure to reduce substantially, a case of Boyle's law (Marshmallow law) where pressure and volume are inversely proportional. With the CO₂ bottle open, CO₂ fills the lines until valves three and four are open to fill the syringe. The filling of CO₂ causes an increase in pressure. When valve three is closed, and valves four and five are then opened, there is a sudden deconfinement or depressurisation, and consequently volume expansion. The result is a rush of the CO₂, which may partly be gaseous CO₂ due to

volume expansion. Given that CO₂ is expected to be refilled at 57 bar (bottle pressure is 57 bar) and the experiment is at 80 bar when it is paused for a refill, one would imagine the 57 bar CO₂ would not bypass the 80 bar CO₂ in the lines when the valves are open to resuming injection. However, it is possible that the entire procedure destabilised the equilibrium and a sudden volume expansion causes CO₂ to bypass the CO₂ in the lines.

Another explanation is that a backflow of CO₂ occurred. The CO₂ that has already bypassed the microchip cools down because it is no longer heated. At room temperature and high pressure of 80 bar, this CO₂ is then liquid. Opening valve five, assuming CO₂ is at 57 bar, allows a backflow as the 80 bar equilibrates with the 57 bar. However, what was observed was the rush of CO₂ into the microchip when valve five was opened, accompanied by a 'pisssss' sound.

Control of the experiment might be gained by changing two things. Either change the refill restart procedure or change the setup design a little. If the plunger of the syringe is withdrawn when valves three and four are open and the CO₂ directly serves the syringe, the pressure decline in the syringe is avoided, like when plunger withdrawal happens with valves 3 and 4 closed. However, this might not solve the lower pressure causing the backflow of CO₂ when 57 bar CO₂ is opened to 80 bar CO₂.

A slight change in the setup design might be the better solution. Using a two syringe pump that injects and refills automatically during the experiments avoids the need for interruption until the end.

Chapter 6

Conclusion

6.1 Summary

Unfortunately, for this thesis time frame, the changes needed to complete the main experiment successfully could not be implemented in time and then continue to steps three and four as described in chapters 4.2.2.3 and 4.2.2.4.

On the other hand, the preliminary experiments demonstrated that salt precipitation is achieved when dry air (gas) is continuously introduced into a saline porous medium. Mechanisms like Two-phase displacement of brine away from the injection point, evaporation of residual brine into the displacing phase, molecular diffusion of dissolved salt into the aqueous phase, and salt self-enhancing lead to and contribute to salt precipitation, as discussed in the literature review chapter.

Mainly, salt precipitated in the dry gas or air phase as polycrystalline crystal aggregates occupying various positions in the edging depth of the micro-model—the aggregates formed in either random shaped patterns or dendritic shaped patterns. Salt also continued to aggregate and self-enhance after the initial aggregate had been created. The permeability of the porous model is expected to reduce, but also, the salt is expected to have some intra-porosity and permeability.

The change in porosity due to the salt precipitation was investigated using ImageJ software and found that with a supersaturated brine, above 25% salt by mass or 250,000 ppm, porosity is reduced by about 20%. However, this result is obtained from a limited brine volume of the experiment. In a real field situation, mechanisms like brine backflow due to salt capillarity would be able to bring in more brine and lead to further precipitation and more porosity reduction.

Considering porosity change alone and looking at the available clogging models for salt precipitation, the power-law and power-law variant models give varying changes in permeability; see Figure 7 (Pruess and Müller, 2009; Verma and Pruess, 1988). These clogging models were constructed on a 'homogeneous layer of salt covering grain surfaces' model or large single salt crystals that precipitate in the aqueous phase and probably do not capture the polycrystalline salt aggregates in the gas phase at the capillary and diffusive regime. This is not realistic as salt aggregation occurs, as seen in the preliminary experiments, and therefore better clogging models are needed.

6.2 Evaluation

The preliminary experiments of this thesis were a success and achieved some of the objectives. The nature of salt crystallisation, the phase in which salt precipitates, some hydraulic properties of the salt, and salt enhancement were investigated.

However, for the main experiment, drying using supercritical CO₂ at reservoir conditions, many technical problems in the setup slowed down the work so that it became impossible to finish all experiments in the set time frame even after numerous extensions. With the suggested changes and experiment procedure, there is high confidence that similar precipitations will be observed, and more hydraulic properties of the salt will be investigated.

6.3 Future Work

Although some questions were answered during the primary investigation, the experiment needs to be completed successfully using supercritical CO₂ under reservoir conditions. The experiment should investigate the impact of salinity, and CO₂ injection rate on salt precipitation patterns and changes in hydraulic properties, especially permeability. Studying permeability changes might give insight into the intrinsic porosity and permeability of the precipitated salt and find a suitable clogging model for salt precipitation.

While I am confident that the experiment will eventually be a success, there will still be limitations to the results and how they might be implemented into numerical simulations. The results of such an experiment are from a limited volume of brine. However, it is expected that brine continues to backflow and cause more salt precipitation than the original residual brine volume would. The so-called brine backflow is enabled by the capillary saturation pressure gradient overcoming the viscous pressure gradient due to strong capillary forces in the salt. However, this experiment's spatial limitation may not achieve such effects. The limited length

(space) scale of the experiment also makes it difficult to investigate the local and heterogeneous salt distribution patterns seen in the literature.

Chapter 7

References

References

André, L., Peysson, Y. and Azaroual, M. (2014) 'Well injectivity during CO₂ storage operations in deep saline aquifers – Part 2: Numerical numerical simulations of drying, salt deposit mechanisms and role of capillary forces', *International Journal of Greenhouse Gas Control*, vol. 22, pp. 301–312.

Arnell, N. W., van Vuuren, D. P. and Isaac, M. (2011) 'The implications of climate policy for the impacts of climate change on global water resources', *Global Environmental Change*, vol. 21, no. 2, pp. 592–603.

Bacci, G., Durucan, S. and Korre, A. (2013) 'Experimental and Numerical Study of the Effects of Halite Scaling on Injectivity and Seal Performance During CO₂ Injection in Saline Aquifers', *Energy Procedia*, vol. 37, pp. 3275–3282.

Bacci, G., Korre, A. and Durucan, S. (2011) 'Experimental investigation into salt precipitation during CO₂ injection in saline aquifers', *Energy Procedia*, vol. 4, pp. 4450–4456.

Bates, N. R. (2019) 'Ocean Carbon Cycle☆', in Cochran, J. K., Bokuniewicz, H. J. and Yager, P. L. (eds) *Encyclopedia of Ocean Sciences (Third Edition)*, Oxford, Academic Press, pp. 418–428.

Bette, S. and Heinemann, R. F. (1989) 'Compositional Modeling of High-Temperature Gas-Condensate Reservoirs With Water Vaporization', *SPE Symposium on Reservoir Simulation*. Houston, Texas, 1989-02-06, Society of Petroleum Engineers.

Carlson, C. A., Bates, N. R., Hansell, D. A. and Steinberg, D. K. (2009) 'Carbon Cycle', in Steele, J. H., Thorpe, S. A. and Turekian, K. K. (eds) *Encyclopedia of ocean sciences*, 2nd edn, San Diego, CA, Academic Press, pp. 477–486.

CHEMYX (2022): *STAINLESS STEEL SYRINGES SPECIFICATIONS* [Online].

CHEMYX, F. 6.-X. (2022) *FUSION 6000-X HIGH PRESSURE SYRINGE PUMP* [Online].

- Fluid Controls Ltd (Dec 22) *Equilibar back pressure regulator gs series* [Online].
- Giorgis, T., Carpita, M. and Battistelli, A. (2007) '2D modeling of salt precipitation during the injection of dry CO₂ in a depleted gas reservoir', *Energy Conversion and Management*, vol. 48, no. 6, pp. 1816–1826.
- (2003) *Green house gas control technologies: 6th international conference*, Amsterdam, Pergamon.
- Grude, S., Landrø, M. and Dvorkin, J. (2014) 'Pressure effects caused by CO₂ injection in the Tubåen Fm., the Snøhvit field', *International Journal of Greenhouse Gas Control*, vol. 27, pp. 178–187.
- Hannah, L. J. (2015) *Climate change biology* [Online], 2nd edn, Amsterdam, Elsevier, Acad. Press. Available at <http://www.sciencedirect.com/science/book/9780124202184>.
- Hansen, O., Gilding, D., Nazarian, B., Osdal, B., Ringrose, P., Kristoffersen, J.-B., Eiken, O. and Hansen, H. (2013) 'Snøhvit: The History of Injecting and Storing 1 Mt CO₂ in the Fluvial Tubåen Fm', *Energy Procedia*, vol. 37, pp. 3565–3573.
- Ho, T.-H. M. and Tsai, P. A. (2020) 'Microfluidic salt precipitation: implications for geological CO₂ storage', *Lab on a chip*, vol. 20, no. 20, pp. 3806–3814.
- Hommel, J., Coltman, E. and Class, H. (2018) 'Porosity–Permeability Relations for Evolving Pore Space: A Review with a Focus on (Bio-)geochemically Altered Porous Media', *Transport in Porous Media*, vol. 124, no. 2, pp. 589–629.
- Hovorka, S. D., Benson, S. M., Doughty, C., Freifeld, B. M., Sakurai, S., Daley, T. M., Kharaka, Y. K., Holtz, M. H., Trautz, R. C., Nance, H. S., Myer, L. R. and Knauss, K. G. (2006) 'Measuring permanence of CO₂ storage in saline formations: the Frio experiment', *Environmental Geosciences*, vol. 13, no. 2, pp. 105–121.
- Intergovernmental Panel on Climate Change (2001) *Climate change 2001: IPCC third assessment report*, Geneva, IPCC Secretariat.
- Intergovernmental Panel on Climate Change (2005) *Carbon Dioxide Capture and Storage*.
- Jasinski, R., Sablerolle, W. and Amory, M. (10051997) 'ETAP: Scale Prediction and Control for the Heron Cluster', *All Days*. San Antonio, Texas, 10/5/1997 - 10/8/1997, SPE.
- Keith Bowman (2016) *The History of Central Mississippi's Naturally Occurring CO₂ Fields* [Online], AAPG (AAPG EXPLORER). Available at <https://explorer.aapg.org/story/articleid/27468/the-history-of-central-mississippi-naturally-occurring-co-fields>.
- KELLER AG für Druckmesstechnik (2021) *Keller Series PRD-33X* [Online].
- Kiessling, D., Schmidt-Hattenberger, C., Schuett, H., Schilling, F., Krueger, K., Schoebel, B., Danckwardt, E. and Kummerow, J. (2010) 'Geoelectrical methods for monitoring geological CO₂ storage: First results from cross-hole and surface–downhole measurements from the CO₂SINK test site at Ketzin (Germany)', *International Journal of Greenhouse Gas Control*, vol. 4, no. 5, pp. 816–826.

Kim, K.-Y., Han, W. S., Oh, J., Kim, T. and Kim, J.-C. (2012) 'Characteristics of Salt-Precipitation and the Associated Pressure Build-Up during CO₂ Storage in Saline Aquifers', *Transport in Porous Media*, vol. 92, no. 2, pp. 397–418.

Kim, M., Sell, A. and Sinton, D. (2013) 'Aquifer-on-a-chip: understanding pore-scale salt precipitation dynamics during CO₂ sequestration', *Lab on a chip*, vol. 13, no. 13, pp. 2508–2518.

Kleinitz, W., Dietzsch, G. and Köhler, M. (2003) 'Halite Scale Formation in Gas-Producing Wells', *Chemical Engineering Research and Design*, vol. 81, no. 3, pp. 352–358.

Lehmann, P. and Or, D. (2009) 'Evaporation and capillary coupling across vertical textural contrasts in porous media', *Physical review. E, Statistical, nonlinear, and soft matter physics*, vol. 80, 4 Pt 2, p. 46318.

Leister Technologies AG (2021) *Mistral 6 system* [Online].

Maldal, T. and Tappel, I. (2004) 'CO₂ underground storage for Snøhvit gas field development', *Energy*, vol. 29, 9-10, pp. 1403–1411.

Masoudi, M., Fazeli, H., Miri, R. and Hellevang, H. (2021) 'Pore scale modeling and evaluation of clogging behavior of salt crystal aggregates in CO₂-rich phase during carbon storage', *International Journal of Greenhouse Gas Control*, vol. 111, p. 103475.

Meng, Q. and Jiang, X. (2014) 'Numerical analyses of the solubility trapping of CO₂ storage in geological formations', *Applied Energy*, vol. 130, pp. 581–591.

MICRONIT (2021) *EOR information: Uniform network, random network and physical rock network* [Online].

Miri, R. and Hellevang, H. (2016) 'Salt precipitation during CO₂ storage—A review', *International Journal of Greenhouse Gas Control*, vol. 51, pp. 136–147.

Miri, R., van Noort, R., Aagaard, P. and Hellevang, H. (2015) 'New insights on the physics of salt precipitation during injection of CO₂ into saline aquifers', *International Journal of Greenhouse Gas Control*, vol. 43, pp. 10–21.

Mito, S. and Xue, Z. (2011) 'Post-Injection monitoring of stored CO₂ at the Nagaoka pilot site: 5 years time-lapse well logging results', *Energy Procedia*, vol. 4, pp. 3284–3289.

Mostafa Borji, B. *Alkali-based Displacement Processes in Microfluidic Experiments: Application to the Matzen Oil Field*.

MOTIC AE2000 BINOCULAR [Online].

Muller, N., Qi, R., Mackie, E., Pruess, K. and Blunt, M. J. (2009) 'CO₂ injection impairment due to halite precipitation', *Energy Procedia*, vol. 1, no. 1, pp. 3507–3514.

Nachshon, U., Weisbrod, N., Dragila, M. I. and Grader, A. (2011) 'Combined evaporation and salt precipitation in homogeneous and heterogeneous porous media', *Water Resources Research*, vol. 47, no. 3.

- Oh, J., Kim, K.-Y., Han, W. S., Kim, T., Kim, J.-C. and Park, E. (2013) 'Experimental and numerical study on supercritical CO₂/brine transport in a fractured rock: Implications of mass transfer, capillary pressure and storage capacity', *Advances in Water Resources*, vol. 62, pp. 442–453.
- Ott, H., Andrew, M., Snippe, J. and Blunt, M. J. (2014) 'Microscale solute transport and precipitation in complex rock during drying', *Geophysical Research Letters*, vol. 41, no. 23, pp. 8369–8376.
- Ott, H., Kloe, K. de, Marcelis, F. and Makurat, A. (2011) 'Injection of supercritical CO₂ in brine saturated sandstone: Pattern formation during salt precipitation', *Energy Procedia*, vol. 4, pp. 4425–4432.
- Ott, H., Roels, S. M. and Kloe, K. de (2015) 'Salt precipitation due to supercritical gas injection: I. Capillary-driven flow in unimodel sandstone', *International Journal of Greenhouse Gas Control*, vol. 43, pp. 247–255.
- Ott, H., Snippe, J. and Kloe, K. de (2021) 'Salt precipitation due to supercritical gas injection: II. Capillary transport in multi porosity rocks', *International Journal of Greenhouse Gas Control*, vol. 105, p. 103233.
- Ott, H., Snippe, J., Kloe, K. de, Husain, H. and Abri, A. (2013) 'Salt Precipitation Due to Sc-gas Injection: Single Versus Multi-porosity Rocks', *Energy Procedia*, vol. 37, pp. 3319–3330.
- Peysson, Y. (2012) 'Permeability alteration induced by drying of brines in porous media', *The European Physical Journal Applied Physics*, vol. 60, no. 2, p. 24206.
- Preston, C., Monea, M., Jazrawi, W., Brown, K., Whittaker, S., White, D., Law, D., Chalaturnyk, R. and Rostron, B. (2005) 'IEA GHG Weyburn CO₂ monitoring and storage project', *Fuel Processing Technology*, vol. 86, 14-15, pp. 1547–1568.
- Pruess, K. and Müller, N. (2009) 'Formation dry-out from CO₂ injection into saline aquifers: 1. Effects of solids precipitation and their mitigation', *Water Resources Research*, vol. 45, no. 3.
- RIDDIFORD, F., TOURQUI, A., BISHOP, C., TAYLOR, B. and SMITH, M. (2003) 'A Cleaner DevelopmentThe in Salah Gas Project, Algeria', in *Green house gas control technologies: 6th international conference*, Amsterdam, Pergamon, pp. 595–600.
- Roels, S. M., El Chatib, N., Nicolaidis, C. and Zitha, P. L. J. (2016) 'Capillary-Driven Transport of Dissolved Salt to the Drying Zone During CO₂ Injection in Homogeneous and Layered Porous Media', *Transport in Porous Media*, vol. 111, no. 2, pp. 411–424.
- S. Parvin, M. Masoudi, A. Sundal, R.Miri (2020) 'Continuum scale modelling of salt precipitation in the context of CO₂ storage in saline aquifers with MRST compositional _ Elsevier Enhanced Reader'.
- Shahidzadeh-Bonn, N., Rafäi, S., Bonn, D. and Wegdam, G. (2008) 'Salt crystallization during evaporation: impact of interfacial properties', *Langmuir : the ACS journal of surfaces and colloids*, vol. 24, no. 16, pp. 8599–8605.

- Shell, C. *QUEST CARBON CAPTURE AND STORAGE* [Online].
- Shell U.K. Limited *Peterhead CCS Project: Stakeholder and Public Engagement and Stakeholder and Public Engagement and Communications Plan* [Online].
- Shokri, N. and Or, D. (2013) 'Drying patterns of porous media containing wettability contrasts', *Journal of colloid and interface science*, vol. 391, pp. 135–141.
- Steele, J. H., Thorpe, S. A. and Turekian, K. K. (eds) (2009) *Encyclopedia of ocean sciences*, 2nd edn, San Diego, CA, Academic Press.
- Torp, T. A. and Gale, J. (2004) 'Demonstrating storage of CO₂ in geological reservoirs: The Sleipner and SACS projects', *Energy*, vol. 29, 9-10, pp. 1361–1369.
- Verma, A. and Pruess, K. (1988) 'Thermohydrological conditions and silica redistribution near high-level nuclear wastes emplaced in saturated geological formations', *Journal of Geophysical Research*, vol. 93, B2, p. 1159.
- Wang, Y. and Liu, Y. (2013) 'Impact of capillary pressure on permeability impairment during CO₂ injection into deep saline aquifers', *Journal of Central South University*, vol. 20, no. 8, pp. 2293–2298.
- Y. Wang, E. Mackie, J. Rohan, T. Luce, R. Knabe and M. Appel (2009) 'Experimental Study on Halite Precipitation During CO₂ Sequestration'.
- Y. Wanga, T. Lucea, C. Ishizawa, M. Shuck, K. Smith, H. Ott and M. Appel (2010) 'Halite Precipitation and Permeability...nt During Supercritical CO₂ Core Flood'.
- he table of contents below is automatically generated by Word. To update this after revisions, right-click in the table and choose “*Update Field*” for the entire table.

